Vibrationally Excited Lines of HC3N Associated with the Molecular Disk around the G24.78+0.08 A1 Hypercompact H ii Region

The Astrophysical Journal, 931:99 (17pp), 2022 June 1 https://doi.org/10.3847/1538-4357/ac69d1

Vibrationally Excited Lines of HC_3N Associated with the Molecular Disk around the G24.78+0.08 A1 Hypercompact H II Region

Kotomi Taniguchi[1], Kei E. I. Tanaka[1,2], Yichen Zhang[3], Rubén Fedriani[4], Jonathan C. Tan[3,4], Shigehisa Takakuwa[5,6], Fumitaka Nakamura[1,7,8], Masao Saito[1,7], Liton Majumdar[9,10], and Eric Herbst[3,11]
[1] National Astronomical Observatory of Japan, National Institutes of Natural Sciences, 2-21-1 Osawa, Mitaka, Tokyo 181-8588, Japan; kotomi.taniguchi@nao.ac.jp, kei.tanaka@colorado.edu
[2] Center for Astrophysics and Space Astronomy, University of Colorado Boulder, Boulder, CO 80309, USA
[3] Department of Astronomy, University of Virginia, Charlottesville, VA 22904, USA
[4] Department of Space, Earth & Environment, Chalmers University of Technology, SE-412 93 Gothenburg, Sweden
[5] Department of Physics and Astronomy, Graduate School of Science and Engineering, Kagoshima University, 1-21-35 Korimoto, Kagoshima, Kagoshima 890-0065, Japan
[6] Academia Sinica Institute of Astronomy and Astrophysics, 11F of Astro-Math Bldg., 1, Section 4 Roosevelt Road, Taipei 10617, Taiwan
[7] Department of Astronomical Science, School of Physical Science, SOKENDAI (The Graduate University for Advanced Studies), Osawa, Mitaka, Tokyo 181-8588, Japan
[8] Department of Astronomy, Graduate School of Science, The University of Tokyo, Hongo, Bunkyo, Tokyo 113-0033, Japan
[9] School of Earth and Planetary Sciences, National Institute of Science Education and Research, Jatni 752050, Odisha, India
[10] Homi Bhabha National Institute, Training School Complex, Anushaktinagar, Mumbai 400094, India
[11] Department of Chemistry, University of Virginia, Charlottesville, VA 22904, USA
Received 2021 December 9; revised 2022 April 20; accepted 2022 April 21; published 2022 May 27

Abstract

We have analyzed Atacama Large Millimeter/submillimeter Array Band 6 data of the hypercompact H II region G24.78+0.08 A1 (G24 HC H II) and report the detection of vibrationally excited lines of HC_3N ($v_7 = 2$, $J = 24 - 23$). The spatial distribution and kinematics of a vibrationally excited line of HC_3N ($v_7 = 2$, $J = 24 - 23$, $l = 2e$) are found to be similar to the CH_3CN vibrationally excited line ($v_8 = 1$), which indicates that the HC_3N emission is tracing the disk around the G24 HC H II region previously identified by the CH_3CN lines. We derive the $^{13}CH_3CN/HC^{13}CCN$ abundance ratios around G24 and compare them to the CH_3CN/HC_3N abundance ratios in disks around Herbig Ae and T Tauri stars. The $^{13}CH_3CN/HC^{13}CCN$ ratios around G24 (∼3.0–3.5) are higher than the CH_3CN/HC_3N ratios in the other disks (∼0.03–0.11) by more than 1 order of magnitude. The higher CH_3CN/HC_3N ratios around G24 suggest that the thermal desorption of CH_3CN in the hot dense gas and efficient destruction of HC_3N in the region irradiated by the strong UV radiation are occurring. Our results indicate that the vibrationally excited HC_3N lines can be used as a disk tracer of massive protostars at the HC H II region stage, and the combination of these nitrile species will provide information of not only chemistry but also physical conditions of the disk structures.

Unified Astronomy Thesaurus concepts: Astrochemistry (75)

1. Introduction

Massive stars (>8 $M_\odot$) play essential roles in the evolution and characterization of galaxies, because they produce and disperse large amounts of energy and heavy elements. However, the formation processes of massive stars remain uncertain (see, e.g., Tan et al. 2014, for a review). One formation scenario is the competitive accretion model, in which massive stars need to form in clustered environments (Bonnell et al. 2001; Wang et al. 2010). Another is the turbulent core accretion model, a scaled-up version of the formation process of low-mass stars (e.g., McKee & Tan 2002, 2003), and which can be applied to both clustered and isolated environments. Theoretical models further investigated stellar feedback from forming massive stars (e.g., disk wind, radiation pressure, photoevaporation, and stellar winds) in the core accretion model (e.g., Tanaka et al. 2016, 2017). In order to reveal the formation process of massive stars and test the theoretical models, high-angular-resolution and high-sensitivity observations are important (Zhang et al. 2019b, 2019c). In particular, observations of molecular lines are essential, because they provide information about not only gas kinematics but also chemical composition, which is an important tracer of physical conditions and evolutionary stage (e.g., Caselli & Ceccarelli 2012; Taniguchi et al. 2019b, 2021b; Jørgensen et al. 2020).

Recent high-angular-resolution observations with interferometers such as the Atacama Large Millimeter/submillimeter Array (ALMA) have revealed the presence of disk structures around O-type and B-type massive protostars (Cesaroni et al. 2017; Maud et al. 2018; Zhang et al. 2019a). Tanaka et al. (2020) detected the high-temperature components of disks, which are located at very close distances to massive protostars (∼100 au scale), using several molecular lines such as H_2O ($v_2 = 1$), NaCl, SiO, and SiS toward the O-type-binary system IRAS 16547–4247 with ALMA. However, the detailed physical and chemical properties of such disk structures around massive protostars are still unclear. The CH_3CN lines are typically used as a disk tracer (Sánchez-Monge et al. 2013; Johnston et al. 2015; Ilee et al. 2016), and sometimes the SiO lines have been used (e.g., Maud et al. 2018; Zhang et al. 2019a).

Nitrile species, CH_3CN and HC_3N, have been frequently detected in disks around Herbig Ae and T Tauri stars (Bergner et al. 2018; Loomis et al. 2018). The Molecules with ALMA at Planet-forming Scale (MAPS; Öberg et al. 2021) Large Program

reveals that these nitrile species trace different layers of these disks; HC_3N traces upper and warmer layers compared to CH_3CN (Ilee et al. 2021). In disks around Herbig Ae and T Tauri stars, CH_3CN is considered to mainly form on dust surfaces followed by the photodesorption or the thermal desorption, while HC_3N forms in the gas phase (Loomis et al. 2018; Le Gal et al. 2019). Based on the rotational temperatures of CH_3CN, the photodesorption is suggested to be more important than the thermal desorption in these disks (Loomis et al. 2018). Hence, it is useful for investigating physical conditions of disks to observe various nitrile species.

In the case of more massive stars, the CH_3CN lines have been frequently used for searching for disks around massive stars (e.g., Johnston et al. 2015; Cesaroni et al. 2017; Sanna et al. 2021), whereas fewer studies about the HC_3N lines have been conducted. The vibrationally excited lines of HC_3N have been detected in compact hot cores around massive protostars (e.g., Wyrowski et al. 1999; Taniguchi et al. 2020), but it was still unclear whether these lines trace massive protostellar disks due to the insufficient angular resolutions of those observations. Other higher-angular-resolution ALMA data (∼400 au) show that an HC_3N vibrationally excited line ($v_7 = 1e$, $J = 38 - 37$; $E_{up}/k = 645$ K) traces an accretion disk around the massive protostar in G328.2551-0.5321 (Csengeri et al. 2018). Their result suggests that the vibrationally excited lines of HC_3N could be a tracer of disks around massive young protostars. In order to confirm this hypothesis, it is essential to investigate massive protostars in various evolutionary stages (e.g., hypercompact H II regions). In addition, the HC_3N chemistry in disk structures around massive protostars has not been discussed yet.

In this paper, we present results of two vibrationally excited HC_3N ($v_7 = 2$, $J = 24 - 23$, $l = 0$, and $l = 2e$) lines detected from the G24.78+0.08 A1 hypercompact H II (hereafter G24 HC H II) region obtained in an ALMA Cycle 6 program. The bolometric luminosity and distance of this source are $\sim 2 \times 10^5$ $L_\odot$ and 6.7 ± 0.7 kpc, respectively (Moscadelli et al. 2021). We adopt a distance of 6.7 kpc to the G24 HC H II region (Moscadelli et al. 2021). This source contains a thin shell ionized by an O9.5 star, which was suggested based on studies of the continuum emission and the hydrogen recombination lines (Cesaroni et al. 2019). Moscadelli et al. (2021) found that CH_3CN lines are consistent with a Keplerian rotation around a 20 $M_\odot$ star along the axis PA = 133° (disk major axis), while an ionized jet has been identified along the axis at PA = 39° at the G24 HC H II region.

The structure of this paper is as follows. We describe the archival data set and reduction procedure in Section 2. The resultant moment 0 maps of the molecular lines are presented in Section 3.1. The position–velocity (P–V) diagrams are constructed and the kinematics of HC_3N and CH_3CN are investigated in Section 3.2. We describe spectral analyses of the $^{13}CH_3CN$ and $HC^{13}CCN$ lines and derive the CH_3CN/HC_3N abundance ratios around the G24 HC H II region in Sections 3.3.1 and 3.3.2, respectively. The CH_3CN/HC_3N ratios in G24 are compared to those in disks around Herbig Ae and T Tauri stars in Section 3.3.3. We will discuss the possibility of a binary system in this source in Section 3.4. In Section 4, the main conclusions of this paper are summarized.

2. ALMA Archival Data and Reduction Procedure

We have analyzed the ALMA Band 6 archival data toward the G24 HC H II region.[12] The observations were conducted using the 12 m array on 2019 July 29 during Cycle 6. Details of the observations are described in Moscadelli et al. (2021).

We conducted data reduction and imaging using the Common Astronomy Software Application (CASA; McMullin et al. 2007) on the pipeline-calibrated visibilities. We ran the calibration script using CASA version 5.6.1. The data cubes were created by the tclean task in CASA. Briggs weighting with a robust parameter of 0.5 was applied. The pixel size and image size are 0.″016 and 3500 × 3500 pixels, respectively. The coordinate of the phase center is (α_{J2000}, δ_{J2000}) = ($18^h36^m12^s.661$, −07°12′10.″15). The maximum baseline length is 8547.6 m. The field of view (FoV) and maximum recoverable scale (MRS) are approximately 26″ and 0.″8, respectively.

Molecular lines and a recombination line presented in this paper are summarized in Table 1. Two vibrationally excited lines of HC_3N ($v_7 = 2$, $J = 24 - 23$, $l = 0$ and $l = 2e$), which are of our main interest, were observed in the same spectral window. These vibrationally excited HC_3N lines have a high upper-state energy of $E_{up}/k \approx 774$–777 K, which makes them suitable for tracing inner hot gas near the central star, i.e., the disk. In addition to the HC_3N lines, we present the data of the CH_3CN ($v_8 = 1$, $J_{K,l} = 12_{6,1} - 11_{6,1}$) line[13] that has a similar upper-state energy to the HC_3N ($v_7 = 2$, $J = 24 - 23$) lines. We will compare their spatial distributions and P–V diagrams in order to confirm that the HC_3N lines trace the disk structure around the G24 HC H II region. We also made data cubes of vibrationally ground-state lines of $^{13}CH_3CN$ ($J_K = 13_K - 12_K$, $K = 0 - 6$) and $HC^{13}CCN$ ($v = 0$, $J = 26 - 25$), which are expected to be optically thin, in order to derive their column densities (Section 3.3.1). The data cube of the H30α line is presented in Section 3.4 to discuss a possibility of the binary system. The velocity resolution of these data is 0.63 km s^{-1}.

A continuum image ($\lambda = 1.38$ mm) was created from the broadest spectral window (1.9 GHz bandwidth, center frequency of 217.8 GHz) using the imcontsub task in CASA. As some lines have been detected at the HC H II region position in this spectral window, we determined line-free channels in the tclean image for

Table 1
Summary of Molecular Lines and a Recombination Line Presented in this Paper

Species	Transition	Frequency (GHz)	E_{up}/k (K)
HC_3N ($v_7 = 2$)[a]	$J = 24 - 23$, $l = 0$	219.6751141	773.5
	$J = 24 - 23$, $l = 2e$	219.7073487	776.8
$HC^{13}CCN$ ($v = 0$)[a]	$J = 26 - 25$	235.5094856	152.6
CH_3CN ($v_8 = 1$)[b]	$J_{K,l} = 12_{6,1} - 11_{6,1}$	221.3118349	771.1
$^{13}CH_3CN$ ($v = 0$)[a]	$J_K = 13_6 - 12_6$	232.0772032	335.5
	$J_K = 13_5 - 12_5$	232.1251297	256.9
	$J_K = 13_4 - 12_4$	232.1643692	192.5
	$J_K = 13_3 - 12_3$	232.1949056	142.4
	$J_K = 13_2 - 12_2$	232.2167263	106.7
	$J_K = 13_1 - 12_1$	232.2298223	85.2
	$J_K = 13_0 - 12_0$	232.2341883	78.0
CH_3CN ($v = 0$)[b]	$J_K = 12_4 - 11_4$	220.6792869	183.1
H30α	⋯	231.900928	⋯

Notes.
[a] The rest frequencies were taken from the Cologne Database for Molecular Spectroscopy (CDMS; Müller et al. 2005).
[b] The rest frequency was taken from the JPL database (Pickett et al. 1998).

[12] Project ID; 2018.1.00745.S, PI; Luca Moscadelli.

[13] The detail studies of this line are summarized in Moscadelli et al. (2021).

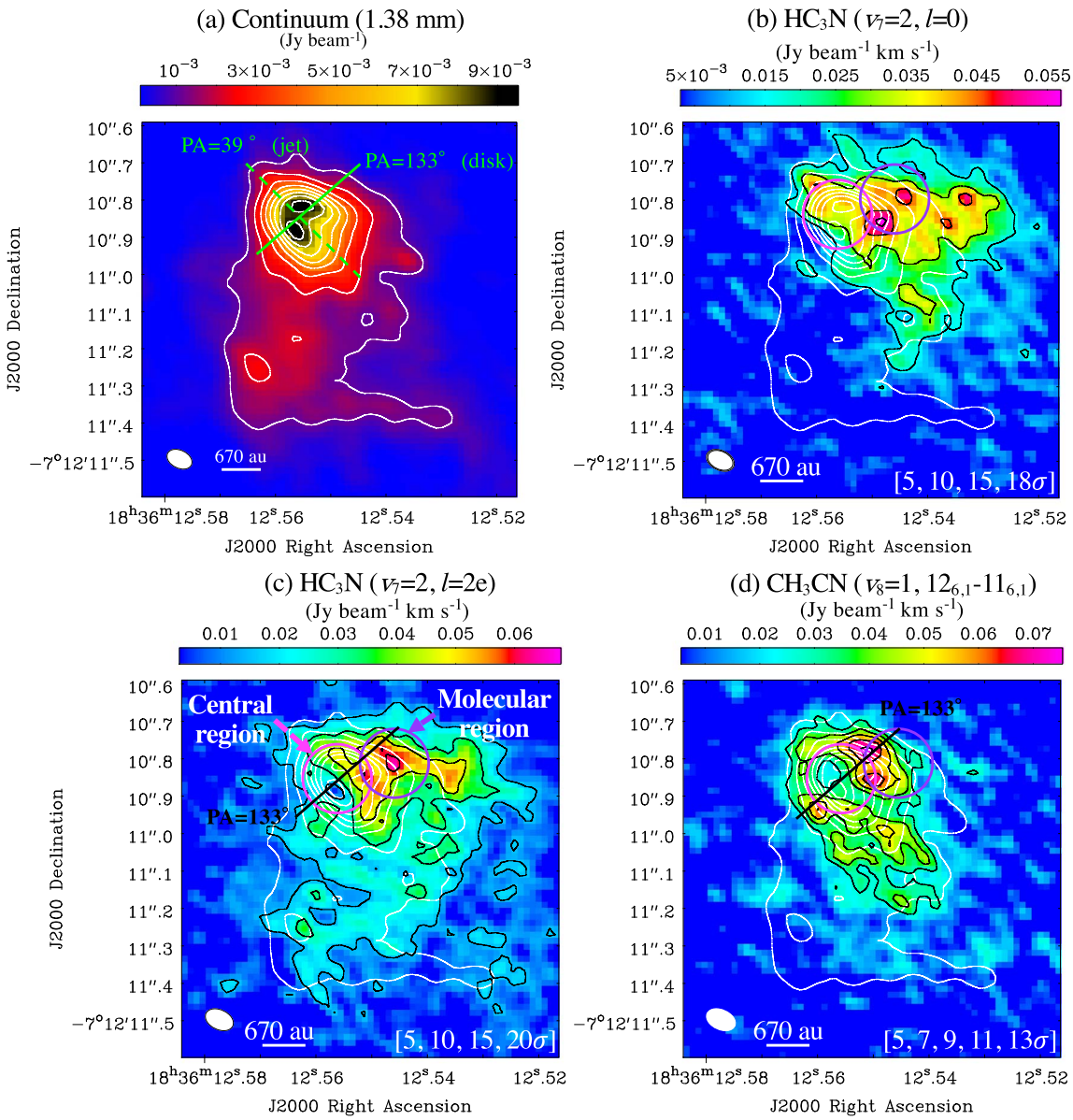

Figure 1. Panel (a) shows the continuum image ($\lambda = 1.38$ mm) toward the G24 HC H II region, which was first reported by Moscadelli et al. (2021). The rms noise level of the image is 0.1 mJy beam^{-1}. The contour levels are 10, 20, 30, 40, 50, 60, 70, 80σ. The filled white ellipse indicates the angular resolution of $0\farcs071 \times 0\farcs048$ and PA = 63.°9. The linear scale is given for $0\farcs1$ corresponding to 670 au. The green solid and dashed lines indicate PA = 133° and PA = 39°, corresponding to the disk major axis and jet directions, respectively (Moscadelli et al. 2021). Panels (b)–(d) show moment 0 images of HC_3N ($v_7 = 2$, $J = 24 - 23$, $l = 0$), HC_3N ($v_7 = 2$, $J = 24 - 23$, $l = 2e$), and CH_3CN ($v_8 = 1$, $J_{K,l} = 12_{6,1} - 11_{6,1}$), respectively, toward the G24 HC H II region. The rms noise levels are 3 mJy beam^{-1} km s^{-1} for panels (b) and (c), and 5.6 mJy beam^{-1} km s^{-1} for panel (d), respectively. The black contour levels are indicated at the right bottom in each panel. The white contours indicate the continuum, which is the same one as panel (a). The filled white ellipses indicate the angular resolutions of $0\farcs079 \times 0\farcs053$ for panels (b) and (c), and $0\farcs082 \times 0\farcs053$ for panel (d), respectively. The linear scale is given for $0\farcs1$ corresponding to 670 au. The magenta and purple circles ($0\farcs1$ radius) indicate the "central region" and "molecular region," respectively. The black lines in panels (c) and (d) indicate the disk major axis (PA = 133°) for the cutting position in the *P*–*V* diagrams (Figure 3).

the imcontsub task. The polynomial order of 0 was adopted for the continuum estimation. The rms noise level of the continuum image is 0.1 mJy beam^{-1}.

3. Results and Discussion

3.1. Spatial Distributions of Molecular Lines

We show the continuum image ($\lambda = 1.38$ mm) toward the G24 HC H II region in panel (a) of Figure 1, which was first reported by Moscadelli et al. (2021). The angular resolution is $0\farcs071 \times 0\farcs048$, corresponding to $\sim$476 au $\times$ 322 au at the source distance of 6.7 kpc. The beam position angle (PA) is 63.°9. Two peaks are located at the center, and the spatial distribution of the continuum emission is slightly elongated along the northeast to southwest direction (PA = 39°). We will discuss a possible reason for the two peaks in the continuum emission in Section 3.4. Another continuum core is located $\sim 0\farcs4$ (2680 au) south of the strongest continuum core. This position is consistent with A1M (a molecular emission peak position) named by Moscadelli et al. (2018), and they found that column densities of several complex organic molecules (COMs) are abundant here.

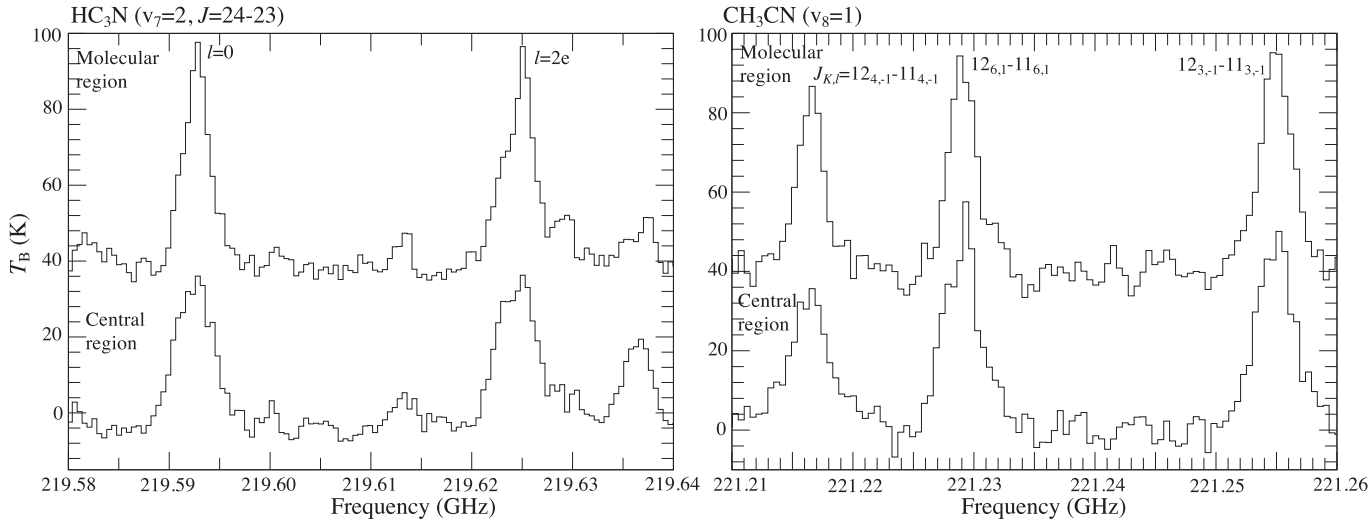

Figure 2. Spectra of the vibrationally excited lines of HC_3N (left panel) and CH_3CN (right panel) at the central and molecular regions obtained by averaging over a $0\farcs1$ radius.

Panels (b)–(d) of Figure 1 show the moment 0 maps of three vibrationally excited molecular lines; (b) HC_3N ($v_7 = 2$, $J = 24 - 23$, $l = 0$), (c) HC_3N ($v_7 = 2$, $J = 24 - 23$, $l = 2e$), and (d) CH_3CN ($v_8 = 1$, $J_{K,l} = 12_{6,1} - 11_{6,1}$); toward the G24 HC H II region. We select two areas for our analysis, namely "central region" and "molecular region" (panel (c) of Figure 1). The central position of the central region corresponds to the middle of the two continuum peaks, and that of the molecular region is at the peak position of the HC_3N ($v_7 = 2$, $J = 24 - 23$, $l = 2e$) line, respectively. Their coordinates are (α_{J2000}, δ_{J2000}) = ($18^h36^m12\fs556$, $-07°12'10\farcs85$), and ($18^h36^m12\fs546$, $-07°12'10\farcs80$), respectively. The other molecular lines also have peaks within the molecular region. We selected the two regions to investigate the potential chemical variation induced by different UV fluxes, which is expected to be higher in the central region. The central region is the same position that Moscadelli et al. (2021) analyzed. Following their work, we adopt the radii of $0\farcs1$ for the two regions, which allows us to check the consistency between their and our analyses (see Section 3.3.1).

Figure 2 shows the spectra of the HC_3N and CH_3CN lines at the central and molecular regions. Other two CH_3CN lines ($v_8 = 1$, $J_{K,l} = 12_{4,-1} - 11_{4,-1}$ and $12_{3,-1} - 11_{3,-1}$) are also detected near the CH_3CN ($v_8 = 1$, $J_{K,l} = 12_{6,1} - 11_{6,1}$) line. We checked molecular lines in the Splatalogue database[14] and found that no other lines are likely to contaminate the spectra. In addition, the two vibrationally excited lines of HC_3N show similar intensities and spatial distributions as expected. We thus concluded that line contamination does not occur.

In the moment 0 maps (panels (b)–(d) of Figure 1), we can recognize the overall similarities in the spatial distributions of the HC_3N and CH_3CN emissions. Their emission regions have similar extents of ~1000 au, because they have almost the same upper-state energies of 771–777 K (Table 1; see also Figure 6 of Moscadelli et al. 2021). Also, all three emissions are dimmer in the central region, probably due to photodissociation by intense UV flux (see also Section 3.3.2). These similarities suggest that the vibrationally excited HC_3N and CH_3CN lines trace the same hot, dense region surrounding the central ionized region, i.e., the molecular disk reported by Moscadelli et al. (2021). We note, despite these similarities, the HC_3N and CH_3CN lines also show a difference in their emission morphology. The CH_3CN emission surrounds the central region, while the two HC_3N lines are mainly located in the northwest. We can explain this spatial difference if the UV flux from the central region is stronger toward the south direction, because HC_3N would be more efficiently photodissociated than CH_3CN (Section 3.3.2). Unresolved asymmetric innermost structures, e.g., clumpy density structure and a presence of a binary system (Section 3.4), could be at the origin of such an anisotropic UV radiation field.

3.2. Kinematics of HC_3N and CH_3CN

Having confirmed the similarity of the spatial distributions, we next investigate the kinematical similarity of the vibrationally excited HC_3N and CH_3CN lines. Moscadelli et al. (2021) reported the Keplerian disk of G24 using the P–V diagrams of the CH_3CN lines, including its vibrationally excited line and ^{13}C isotopologue line. In order to confirm that the vibrationally excited HC_3N line also traces the same molecular disk, we constructed P–V diagrams of HC_3N ($v_7 = 2$, $J = 24 - 23$, $l = 2e$) and CH_3CN ($v_8 = 1$, $J_{K,l} = 12_{6,1} - 11_{6,1}$) along the disk major axis of PA = 133° (shown in Figure 1). We used "impv" task in CASA and averaged the emission over three pixels across the positional cut. The center position (offset = 0″) is set at the coordinate of the central region. Panels (a) and (b) of Figure 3 show the P–V diagrams of the vibrationally excited HC_3N and CH_3CN lines, respectively. Their channel maps are shown in Figures 11 and 12 in Appendix B. For comparison, we also provide the P–V diagram of the vibrational ground-state line of CH_3CN ($J_K = 12_4 - 11_4$), which clearly shows the Keplerian feature with $20\,M_\odot$ but becomes dimmer in the innermost region (panel (c) of Figure 3).

In the P–V diagrams, we could confirm that the HC_3N emission has kinematic similarities with the vibrationally excited and ground-state CH_3CN lines, but the resemblance is stronger to the vibrationally excited line of CH_3CN. The brightest features appear in the northwest and redshifted side, and the dimmest features are in the northwest and blueshifted side in all three panels of Figure 3. On the brightest side, the HC_3N emission covers the innermost region of $+0\farcs0$ to $+0\farcs1$ like the vibrationally excited CH_3CN line, which has almost the

[14] https://splatalogue.online//advanced1.php

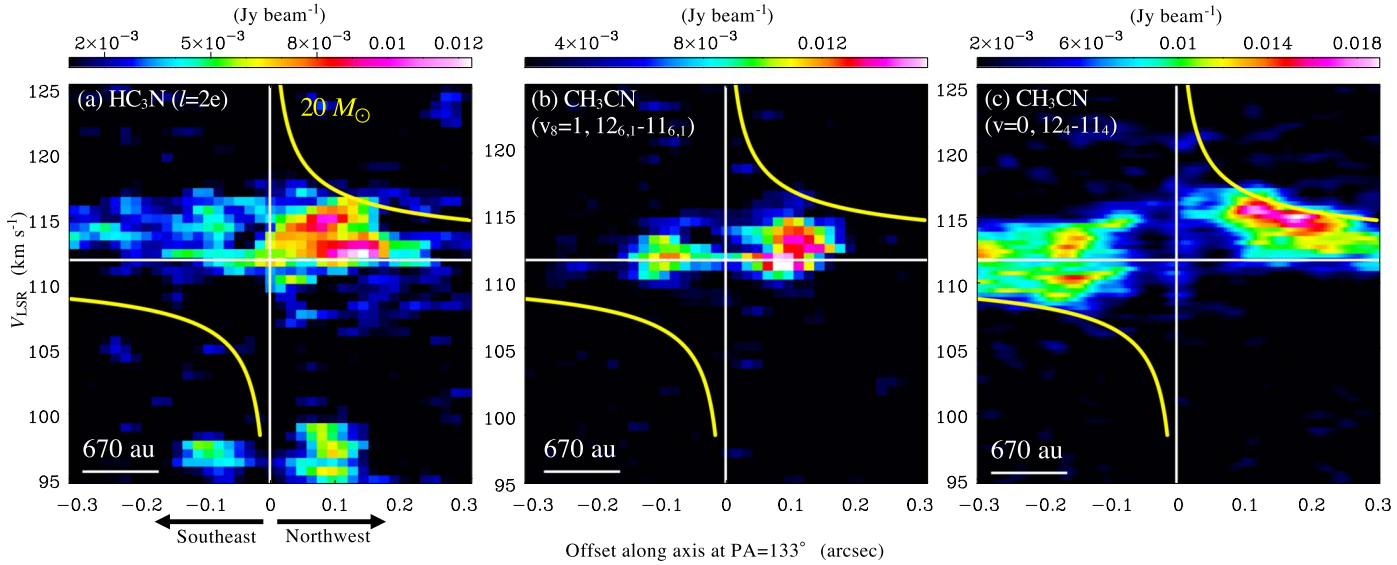

Figure 3. *P–V* diagrams of (a) HC_3N ($v_7 = 2$, $J = 24 - 23$, $l = 2e$), (b) CH_3CN ($v_8 = 1$, $J_{K,l} = 12_{6,1} - 11_{6,1}$), and (c) CH_3CN ($v = 0$, $J_K = 12_4 - 11_4$) along the cut at PA = 133° (the disk major axis). The horizontal white lines indicate $V_{LSR} = 112$ km s^{-1}, which is the systemic velocity of the G24 HC H II region (Moscadelli et al. 2021). The offset center (offset = 0″) corresponds to the center of the HC H II region. The positive and negative offsets correspond to northwest and southeast directions, respectively. The yellow lines indicate the Keplerian velocity profile for a central mass of 20 $M_\odot$ (the disk inclination is not taken into account).

same upper-state energy (panels (a) and (b)). Moreover, on the same side, the HC_3N emission shows the consistent profile as the Keplerian rotation seen in the ground-state CH_3CN emission (panels (a) and (c)). Hence, we conclude that the vibrationally excited HC_3N line is associated with the same Keplerian disk reported by Moscadelli et al. (2021). Although the HC_3N emission shows some resemblance to that of CH_3CN in the *P–V* diagrams (Figure 3), the degree of this resemblance is still debatable. Future higher-angular-resolution observations including other transitions are necessary for further discussions.

The other similarity is that these HC_3N and CH_3CN lines show emission features on the southeast and redshifted side of the *P–V* diagrams (see also Figure 4 of Moscadelli et al. 2021). The distribution of the HC_3N emission lines is intermediate between those of the vibrationally excited and ground-state CH_3CN lines. This again supports that the HC_3N line traces the same gas as CH_3CN. We note that such a kinematical feature cannot be reproduced by a pure Keplerian disk (Sakai et al. 2014; Zhang et al. 2019a). Contamination from an infalling, rotating envelope is able to create this feature, even though we used the lines with the high upper-state energies, which can be excited only in hot dense gas (see $E_{up}/k = 777$ K and the critical density of $\gtrsim 4 \times 10^8$ cm^{-3} for the HC_3N line; Wyrowski et al. 1999). One difference between the HC_3N and ground-state CH_3CN lines appears on the southeast and blueshifted sides in their *P–V* diagrams (panels (a) and (c)). The HC_3N emission is darker on the southeast side, making it difficult to trace that side of the Keplerian feature (see also Figure 1). An anisotropic UV radiation field could create this HC_3N depletion, which we also mentioned in Section 3.1. This would imply that fast chemical processes change the chemical composition of the molecular disk with a shorter timescale than the rotational timescale for the disk (e.g., Cleeves et al. 2017).

3.3. The Abundances of HC_3N and CH_3CN

As mentioned in Section 1, HC_3N and CH_3CN trace different layers of disks around Herbig Ae and T Tauri stars (Ilee et al. 2021), suggesting that these species trace different physical conditions in disk structures. In order to investigate the physical and chemical conditions of the molecular disk around the G24 HC H II region, we will evaluate the CH_3CN/HC_3N abundance ratios.

3.3.1. Spectral Line Analyses of $^{13}CH_3CN$ and $HC^{13}CCN$

We derive column densities of $HC^{13}CCN$ and $^{13}CH_3CN$ using their vibrational ground-state lines. Figure 10 in Appendix A shows the moment 0 maps of the vibrational ground-state lines of their ^{13}C isotopologues. These lines are usually optically thin, and we can derive their column densities more accurately than the case with the main species.

We obtained the spectra of $^{13}CH_3CN$ and $HC^{13}CCN$ at the central and molecular regions over the 0.″1 radius. As described in Section 3.1, the central region is the same region where Moscadelli et al. (2021) analyzed. The derived column densities and rotational temperatures in this section are the beam-averaged values, as Moscadelli et al. (2021) derived.

Panels (a) and (b) of Figure 4 show the spectra of $^{13}CH_3CN$ ($J = 13 - 12$) at the central and molecular regions, respectively. We fitted the spectra with a Gaussian profile and summarized the obtained parameters in Table 2. We analyzed the $^{13}CH_3CN$ spectra with the rotational diagram method using the following formula (Goldsmith & Langer 1999);

$$\ln \frac{3k \int T_B dv}{8\pi^3 \nu S \mu^2} = \ln \frac{N}{Q(T_{rot})} - \frac{E_{up}}{kT_{rot}}, \quad (1)$$

where k is the Boltzmann constant, S is the line strength, μ is the permanent electric dipole moment, N is the column density, T_{rot} is the rotational temperature, E_{up} is the upper-state energy, and $Q(T_{rot})$ is the partition function. The permanent electric dipole moment of $^{13}CH_3CN$ is 3.92197 Debye (Gadhi et al.1995).

Panels (c) and (d) of Figure 4 show results of the rotational diagram analysis at the central and molecular regions, respectively. At the central region, we could not obtain the rotational temperature by the fitting, partly because some lines do not show a Gaussian profile, and then we applied a

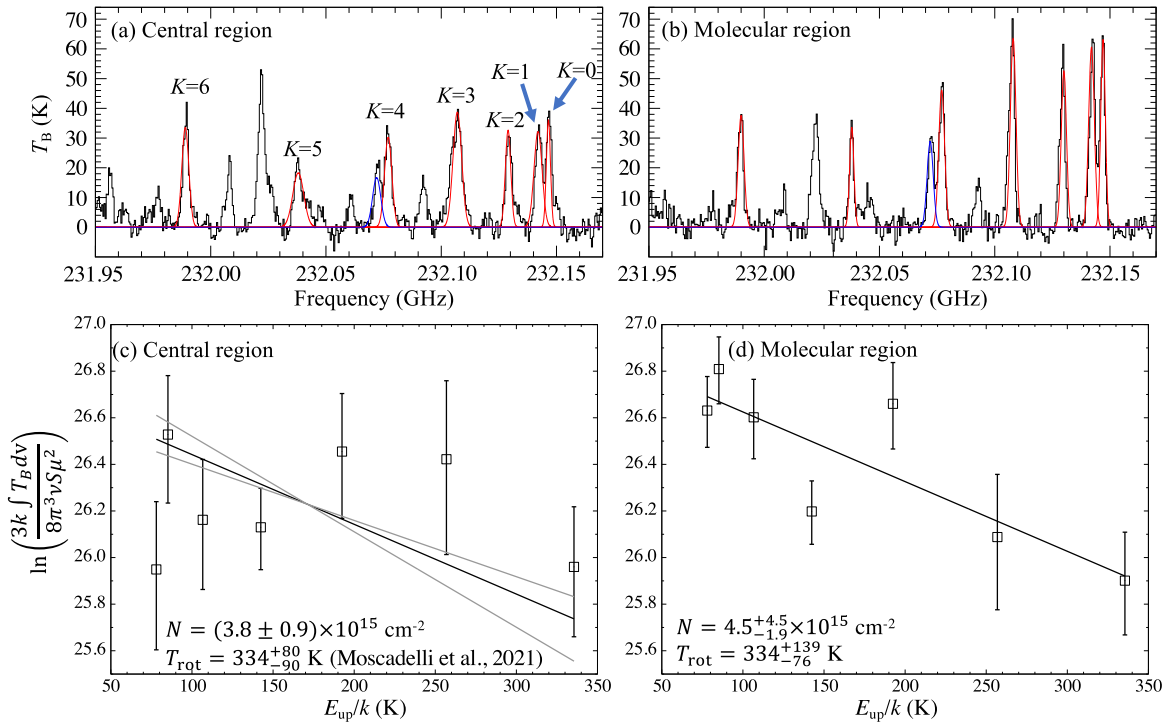

Figure 4. Spectra of $^{13}CH_3CN$ obtained by averaging over a 0.″1 radius at the center of the central and molecular regions in panels (a) and (b), respectively. Red curves show the Gaussian fitting results for the $^{13}CH_3CN$ lines, and blue curves indicate the fit results for a line from another molecule (we could not clearly identify a molecule and its transition because of a possibility of line contamination). Panels (c) and (d) show results of the rotational diagram fit at the central and molecular regions, respectively. The error bars for each data point are derived from the standard deviation of the line fitting with a Gaussian profile summarized in Table 2. In panel (c), the black line shows the fitting result to our data using $T_{rot} = 334$ K, and the gray lines indicate the fitting results to our data using $T_{rot} = (334 + 80)$ K and $T_{rot} = (334 - 90)$ K.

Table 2
Gaussian Fitting Results of the $^{13}CH_3CN$ and $HC^{13}CCN$

Line	Central Region		Molecular Region	
	T_B (K)	Δv (km s^{-1})	T_B (K)	Δv (km s^{-1})
		$^{13}CH_3CN$ ($J_K = 13_K - 12_K$)		
$K = 0$	36.0 ± 4.4	2.7 ± 0.5	63.1 ± 3.7	3.0 ± 0.3
$K = 1$	32.1 ± 3.1	5.4 ± 0.9	60.6 ± 3.4	3.8 ± 0.3
$K = 2$	32.6 ± 3.8	3.6 ± 0.6	52.6 ± 3.7	3.5 ± 0.3
$K = 3$	38.7 ± 3.0	5.7 ± 0.5	63.5 ± 3.7	3.7 ± 0.3
$K = 4$	30.2 ± 3.3	4.8 ± 0.8	46.1 ± 3.4	3.9 ± 0.4
$K = 5$	18.3 ± 2.7	7.3 ± 1.6	33.6 ± 3.9	2.8 ± 0.5
$K = 6$	33.5 ± 3.4	4.6 ± 0.8	37.6 ± 3.4	3.9 ± 0.5
		$HC^{13}CCN$ ($J = 26 - 25$)		
$J = 26 - 25$	33.4 ± 1.7	6.0 ± 0.4	58.1 ± 3.0	4.6 ± 0.3

Note. Errors indicate the standard deviation.

rotational temperature of 334^{+80}_{-90} K derived by Moscadelli et al. (2021). Their results are applicable, as Moscadelli et al. (2021) analyzed the $^{13}CH_3CN$ spectra at the HC H II region within a 0.″1 radius, which is the same region as we have analyzed. The column density of $^{13}CH_3CN$ at the HC H II region is derived to be $(3.8 \pm 0.9) \times 10^{15}$ cm^{-2}. This column density is consistent with the previous result within the uncertainties ($5.01^{+1.2}_{-1.5} \times 10^{15}$ cm^{-2}; Moscadelli et al. 2021). The rotational temperature and column density at the molecular region are derived to be 334^{+139}_{-76} K and $4.5^{+4.5}_{-1.9} \times 10^{15}$ cm^{-2}, respectively, by the rotational diagram fitting for our data.

The derived rotational temperatures at the two positionsare much higher than the sublimation temperature of CH_3CN (≈95 K[15]), which is different from results in the disks around the Herbig Ae and T Tauri stars (Bergner et al. 2018; Loomis et al. 2018; Ilee et al. 2021). Such high rotational temperatures of $^{13}CH_3CN$ indicate that CH_3CN, including its isotopologues, thermally desorbs from dust grains rather than photodesorption by the UV radiation around the G24 HC H II region.

[15] We took the sublimation temperature from a hot-core model by Taniguchi et al. (2019a).

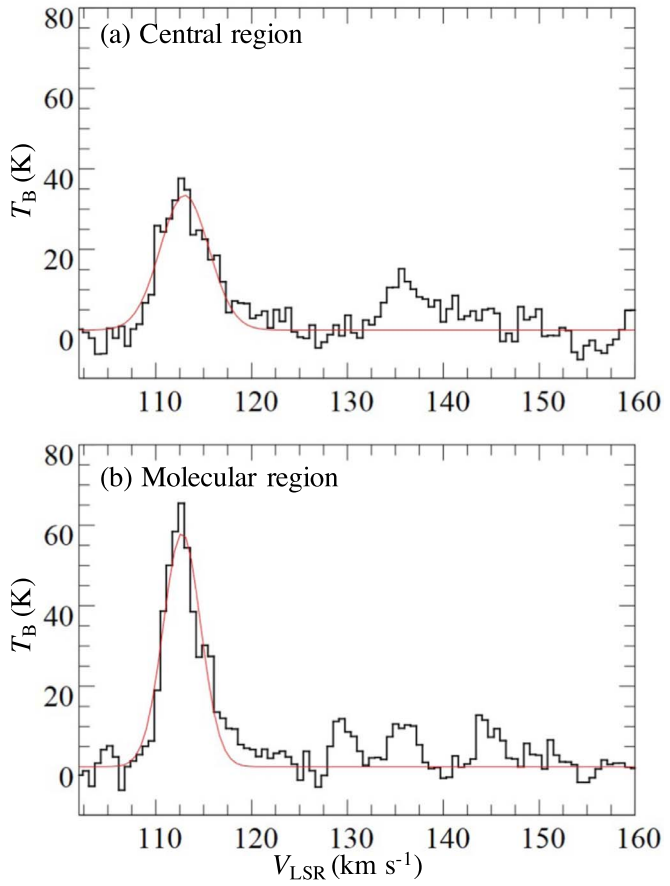

Figure 5. Spectra of HC^{13}CCN ($J = 26 - 25$) obtained by averaging over a 0.″1 radius at the center of the central and molecular regions in panels (a) and (b), respectively. The red curves show the results of the Gaussian fit.

Figure 5 shows spectra of the HC^{13}CCN ($J = 26 - 25$) line at the central and molecular regions, obtained by the same method as that for $^{13}CH_3CN$. We fitted the spectra with a Gaussian profile, and the fitting results are shown as red curves in Figure 5. Table 2 summarizes the line parameters obtained by the fitting. The V_{LSR} values of this line are 113.0 ± 0.15 km s^{-1} and 112.7 ± 0.12 km s^{-1} at the central and molecular regions, respectively.

As we have only one rotational transition line of HC^{13}CCN, we need a reasonable assumption of its excitation temperature to derive its column density. If the emission region of $^{13}CH_3CN$ coincides with that of HC^{13}CCN and the local thermodynamic equilibrium (LTE) condition is achieved, we can use the excitation temperature of $^{13}CH_3CN$ as the reference value. Therefore, we compare their line widths of $^{13}CH_3CN$ and HC^{13}CCN to examine their spatial coincidence.

Figure 6 shows relationships between the FWHM and the upper-state energy of the $^{13}CH_3CN$ and HC^{13}CCN lines. We derive the FWHM using

$$\mathrm{FWHM} = \sqrt{(\Delta v_{\mathrm{obs}})^2 - (\Delta v_{\mathrm{inst}})^2}, \quad (2)$$

where Δv_{obs} and Δv_{inst} are the observed line widths and the instrumental velocity width (0.63 km s^{-1}), respectively. There are no clear dependencies of the line width on the upper-state energy. The value of the $K = 5$ line of $^{13}CH_3CN$ and its error toward the central region are slightly larger than those of the other lines, which may be due to the contamination of another line (panel (a) of Figure 4). The line widths at the central region are generally larger than those at the molecular region, and the line widths of the HC^{13}CCN line are comparable to those of $^{13}CH_3CN$. Thus, we hereafter assume the excitation temperature of HC^{13}CCN is the same as the $^{13}CH_3CN$'s rotational temperature.

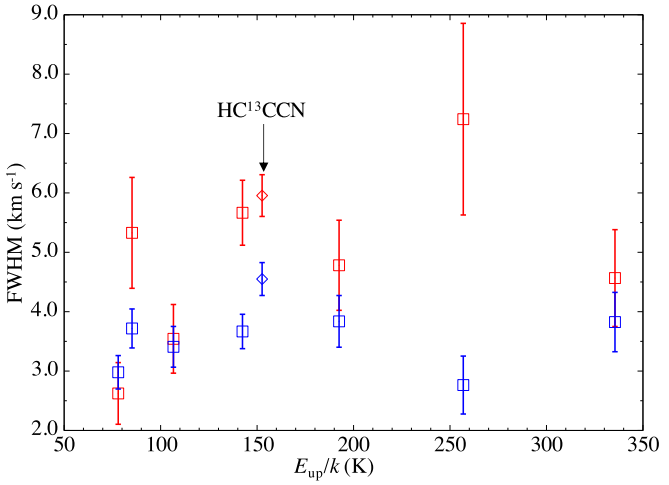

Figure 6. Plot of the upper-state energy (E_{up}) vs. the FWHM of the $^{13}CH_3CN$ and HC^{13}CCN lines. The red and blue plots represent data points of the central and molecular regions, respectively. The square and diamond signs indicate the $^{13}CH_3CN$ and HC^{13}CCN data, respectively.

We derived the column densities of HC^{13}CCN at the two positions assuming the LTE condition (Goldsmith & Langer 1999). We used the following formulae;

$$\tau = -\ln\left[1 - \frac{T_B}{J(T_{ex}) - J(T_{bg})}\right], \quad (3)$$

where

$$J(T) = \frac{h\nu}{k}\left\{\exp\left(\frac{h\nu}{kT}\right) - 1\right\}^{-1}, \quad (4)$$

and

$$N = \tau \frac{3h\Delta v}{8\pi^3}\sqrt{\frac{\pi}{4\ln 2}}\,Q(T_{ex})\frac{1}{\mu^2}\frac{1}{J_{lower}+1} \times \exp\left(\frac{E_{lower}}{kT_{ex}}\right)\left\{1 - \exp\left(-\frac{h\nu}{kT_{ex}}\right)\right\}^{-1}. \quad (5)$$

In Equation (3), τ denotes the optical depth, and T_B the peak intensities summarized in Table 2. T_{ex} and T_{bg} are the excitation temperature and the cosmic microwave background temperature (2.73 K). We calculated three cases of excitation temperatures (T_{ex}, $T_{ex} \pm T_{ex}$(error)) for each position. $J(T)$ in Equation (4) is the effective temperature equivalent to that in the Rayleigh–Jeans law. In Equation (5), N is the column density, Δv is the line width, $Q(T_{ex})$ is the partition function at T_{ex}, μ is the permanent electric dipole moment, and E_{lower} is the energy of the lower rotational energy level. The electric dipole moment of HC^{13}CCN is 3.732 Debye (CDMS database; Müller et al. 2005).

Table 3 summarizes the derived column densities of HC^{13}CCN and the peak optical depth (τ) at each position. We confirmed that the HC^{13}CCN line is optically thin. The derived column densities at the molecular region are slightly higher than those at the central region, as in the case of $^{13}CH_3CN$ (see Figure 4).

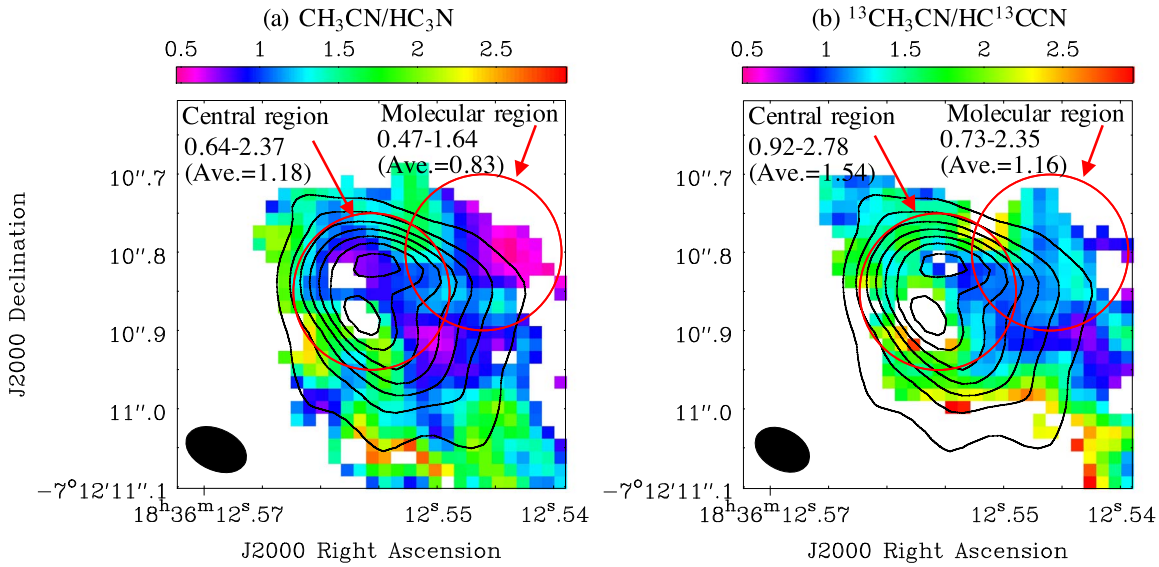

Figure 7. Maps of the moment 0 ratios between (a) CH_3CN ($v_8 = 1$, $J_{K,l} = 12_{6,1} - 11_{6,1}$) and HC_3N ($v_7 = 2$, $J = 24 - 23$, $l = 2e$) (panels (d) and (c) of Figure 1, respectively) and (b) $^{13}CH_3CN$ ($J_K = 13_3 - 12_3$) and $HC^{13}CCN$ ($J = 26 - 25$) (panels (c) and (a) of Figure 10, respectively) toward G24. The red circles represent the central and molecular regions. The indicated values are minimum, maximum, and average values in each region. The average values are calculated based on the total fluxes in each moment 0 map. The black contours indicate the continuum emission from 20σ to 80σ.

Table 3
Column Density and Optical Depth of $HC^{13}CCN$

Central Region			Molecular Region		
T_{ex} (K)[a]	N (cm^{-2})	τ	T_{ex} (K)[a]	N (cm^{-2})	τ
334	$(1.08 \pm 0.08) \times 10^{15}$	0.107	334	$(1.48 \pm 0.12) \times 10^{15}$	0.195
244	$(9.4 \pm 0.7) \times 10^{14}$	0.151	258	$(1.36 \pm 0.11) \times 10^{15}$	0.262
414	$(1.20 \pm 0.09) \times 10^{15}$	0.086	473	$(1.78 \pm 0.14) \times 10^{15}$	0.133

Notes. Errors indicate the standard deviation.
[a] Excitation temperatures (T_{ex}) are taken from the results of $^{13}CH_3CN$.

3.3.2. The CH_3CN/HC_3N Abundance Ratios in G24

The $N(^{13}CH_3CN)/N(HC^{13}CCN)$ ratios are derived to be 3.47 ± 0.46 and $3.10^{+3.68}_{-1.62}$ at the central and molecular regions, respectively, using the results in Section 3.3.1. If there are no effects of the ^{13}C isotopic fractionation in each molecule (e.g., Taniguchi et al. 2016, 2017) and the selective photodissociation of $^{13}CH_3CN$ and $HC^{13}CCN$, the $N(^{13}CH_3CN)/N(HC^{13}CCN)$ ratio reflects the CH_3CN/HC_3N abundance ratio. In the case of G24 with the strong UV radiation field, it is likely that the effect of the ^{13}C isotopic fractionation of HC_3N is negligible (Taniguchi et al. 2019a, 2021a).

In order to confirm the CH_3CN/HC_3N abundance ratios around G24, we investigated the CH_3CN/HC_3N ratios using the moment 0 maps of their vibrationally excited lines. These lines have similar upper-state energies (~770 K, Table 1). In addition, the estimated gas density traced by the CH_3CN ($v_8 = 1$) lines is around 10^9 cm^{-3} (Moscadelli et al. 2021), and the critical density of the HC_3N ($v_7 = 2$) lines is $\geqslant 4 \times 10^8$ cm^{-3} (Wyrowski et al. 1999). Hence, these vibrationally excited lines of CH_3CN and HC_3N likely trace similar regions around G24, and their excitation conditions are expected to be equivalent. If these lines are optically thin, this integrated-intensity ratio would be comparable to their abundance ratio. Panel (a) of Figure 7 shows the map of the ratio between the CH_3CN moment 0 map (panel (d) of Figure 1) and that of HC_3N (panel (c) of Figure 1) toward G24. We included only pixels with above 3σ detection of both species. We also show the same map but between the $^{13}CH_3CN$ ($J_K = 13_3 - 12_3$) and $HC^{13}CCN$ ($J = 26 - 25$) lines (panels (c) and (a) of Figure 10, respectively), in order to cross check the results. We used the $^{13}CH_3CN$ ($J_K = 13_3 - 12_3$) line, because it has the closest upper-state energy to the $HC^{13}CCN$ ($J = 26 - 25$) line (see Table 1).

The CH_3CN/HC_3N ratios including their ^{13}C isotopologues cannot be derived near the continuum peak due to the below 3σ detection of HC_3N, which could indicate the efficient HC_3N destruction at the central region. In panel (a), the CH_3CN/HC_3N ratio shows lower values in the molecular region (≈0.5–1.6, the average value is 0.83) compared to those in the central region (≈0.6–2.4, the average value is 1.18). This marginal difference in the CH_3CN/HC_3N ratio between the two regions suggests that the UV photodissociation and/or reactions with ions increase the CH_3CN/HC_3N abundance ratio in the region irradiated by the strong UV radiation. This can be caused by the following two reasons;

1. HC_3N could be more efficiently destroyed at the central region, because the UV photodissociation rate of HC_3N is

higher than that of CH_3CN by a factor of ∼2.4 (Table 2 in Le Gal et al. 2019).

2. HC_3N is destroyed by reactions with ions (H^+, H_3^+, HCO^+), which should be abundant in ionized regions (Taniguchi et al. 2019a).

The $^{13}CH_3CN/HC^{13}CCN$ ratios are derived to be ≈0.9–2.8 (the average value is 1.54) and ≈0.7–2.4 (the average value is 1.16) at the central and molecular regions, respectively (panel (b) of Figure 7). The $^{13}CH_3CN/HC^{13}CCN$ ratio at the molecular region is lower than that at the central region, as seen in panel (a), and this tendency is also consistent with the $N(^{13}CH_3CN)/N(HC^{13}CCN)$ ratios.

We adopt the $N(^{13}CH_3CN)/N(HC^{13}CCN)$ column density ratio as representative values in G24 in the following section, because the CH_3CN/HC_3N ratio based on the moment 0 maps may be affected by the effect of the optically thickness.

3.3.3. Comparisons of the CH_3CN/HC_3N Abundance Ratios Among the High- and Lower-mass Protostellar Disks

We compare the CH_3CN/HC_3N abundance ratios in the disk structure of G24 to those in disks around lower-mass stars, i.e., Herbig Ae stars and T Tauri stars, and investigate chemical properties of the molecular disk around G24.

In disks around lower-mass stars, a main formation mechanism of CH_3CN is considered to be dust-surface reactions (Bergner et al. 2018; Loomis et al. 2018); (1) the successive hydrogenation reaction of C_2N and (2) a radical–radical reaction between CH_3 and CN. Gas-phase routes have been also investigated (Bergner et al. 2018; Loomis et al. 2018):

$$CH_3^+ + HCN \rightarrow (CH_3NCH^+)^* \rightarrow CH_3CNH^+ + h\nu, \quad (6)$$

followed by

$$CH_3CNH^+ + e^- \rightarrow CH_3CN + H. \quad (7)$$

However, Loomis et al. (2018) concluded that the dust-surface routes are more efficient than the gas-phase ones. The CH_3CN formed on dust surfaces sublimates into the gas phase by thermal desorption or photoevaporation. As the excitation temperatures of CH_3CN are lower than its sublimation temperature in disks around lower-mass stars, the primary path would be photoevaporation in such disks.

On the other hand, for HC_3N, only gas-phase formation routes are known, including the ion–molecule reactions and the neutral–neutral reactions (Loomis et al. 2018; Le Gal et al. 2019). For example, the following reactions are considered to contribute to the HC_3N formation:

$$HC_3NH^+ + e^- \rightarrow HC_3N + H \quad (8)$$

or

$$C_2H_2 + CN \rightarrow HC_3N + H. \quad (9)$$

The HC_3NH^+ ion is formed by various ion–molecule reactions (e.g., $C_2H_2^+ + HCN$, $C_3H_n^+ + N$ ($n = 3, 4, 5$); Taniguchi et al. 2016, 2017).

Both CH_3CN and HC_3N are destroyed by the UV photodissociation:

$$CH_3CN + h\nu \rightarrow CH_3 + CN \quad (10)$$

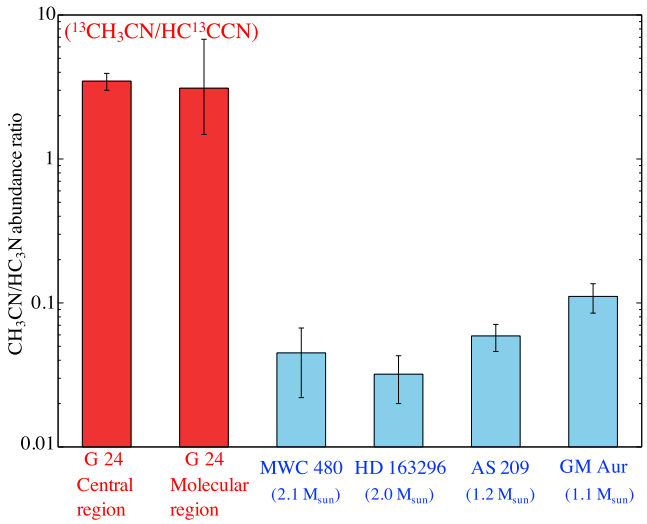

Figure 8. Comparisons of the CH_3CN/HC_3N abundance ratio among disks with different stellar masses. Values except for G24 are taken from Ilee et al. (2021). The stellar masses of Herbig Ae and T Tauri stars are taken from Öberg et al. (2021).

and

$$HC_3N + h\nu \rightarrow CCH + CN, \quad (11)$$

respectively. HC_3N is also destroyed by ions, such as H^+, H_3^+, HCO^+, in higher A_v regimes ($A_v \gtrsim 4$ mag; Le Gal et al. 2019). The reaction with C^+ could destroy CH_3CN (Loomis et al. 2018), but its contribution is not dominant in the chemical network simulation conducted by Le Gal et al. (2019).

Figure 8 shows comparisons of the CH_3CN/HC_3N abundance ratio among protostellar disks with different stellar masses. The abundance ratios in Herbig Ae and T Tauri stars are taken from Ilee et al. (2021). MWC 480 and HD 163296 are Herbig Ae stars, and AS 209 and GM Aur are T Tauri stars, respectively. The derived $N(^{13}CH_3CN)/N(HC^{13}CCN)$ ratios around G24 (∼3.0–3.5) are higher than the CH_3CN/HC_3N abundance ratios in the other disks (∼0.03–0.11) by more than 1 order of magnitude. As discussed in Section 3.3.2, there are differences in the CH_3CN/HC_3N ratio around the G24 HC H II region by a factor of a few among different methods, but the CH_3CN/HC_3N ratios around G24 are clearly higher than those in the disks around the lower-mass stars.

One possible explanation for the high CH_3CN/HC_3N abundance ratio around G24 is that the thermal sublimation mechanism enhances the gas-phase CH_3CN abundance around the massive star, while the photoevaporation is important for sublimation of CH_3CN in the other disks. In addition, HC_3N could be more efficiently destroyed around the massive star, because of the higher UV photodissociation rate of HC_3N than that of CH_3CN, as we have already discussed in Section 3.3.2. HC_3N is also destroyed by reactions with ions (H^+, H_3^+, HCO^+), which should be abundant in ionized regions.

We also compare the CH_3CN/HC_3N ratios around G24 to that of the Orion Hot Core (i.e., envelope scale; Crockett et al. 2014). The Orion Hot Core is associated with Source I, and its mass was estimated to be around 15 $M_\odot$ (Bally et al. 2020). In addition, the disk structure has been detected around this source (Wright et al. 2020). Thus, it seems to be a good source to compare the chemical composition to G24. The CH_3CN and HC_3N abundances with respect to H_2 at the Orion Hot Core

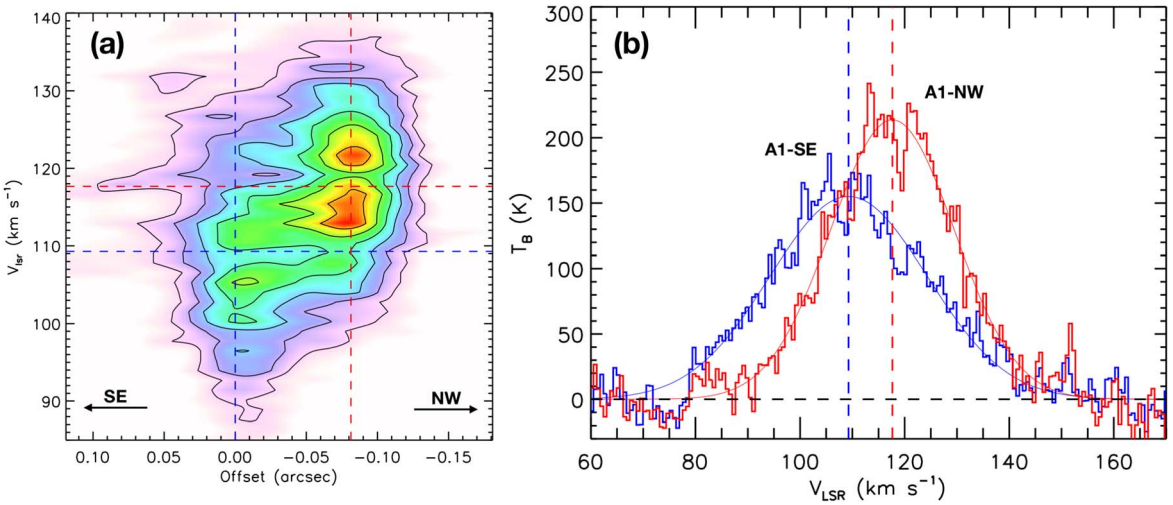

Figure 9. (a) Position–velocity diagram of the H30α emission along a strip connecting the two continuum peaks with a width of 0.″01. The dashed lines in blue and red colors mark the locations and center velocities of the southeast peak and the northwest peak, respectively. (b) H30α spectra at the two continuum peak positions (blue: southeast peak, named as A1-SE; red: northwest peak, named as A1-NW). The solid thin lines show the Gaussian fitting to the spectra, with the central velocities marked by the vertical dashed lines ($v_{\rm center} = 109.3 \pm 0.3$ km s^{-1} for A1-SE and $v_{\rm center} = 117.7 \pm 0.2$ km s^{-1} for A1-NW).

were derived to be 3.0×10^{-8} and 8.1×10^{-9}, respectively ($N(H_2) = 3.1 \times 10^{23}$ cm^{-2}; Crockett et al. 2014). Hence, the CH_3CN/HC_3N abundance ratio is calculated at 3.7. This value is comparable to the CH_3CN/HC_3N ratios around G24 (~3.0–3.5). The similar CH_3CN/HC_3N ratios between the central and molecular regions in G24, and between G24 and the Orion Hot Core imply the following two possibilities:

1. The disk chemistry may be inherited from the envelope.
2. The chemical processes at the envelope scale may be similar to those at the disk scale due to the powerful central source.

Here, we demonstrate the possibility of the different nitrile chemistry between massive stars and lower-mass stars, i.e., Herbig Ae and T Tauri stars. However, we have data of both CH_3CN and HC_3N toward only one massive star. In order to confirm the nitrile chemistry in disk structures around massive stars, we need to increase source samples. Future observations covering several lines, which enable us to derive accurate column densities and excitation temperatures of CH_3CN and HC_3N, are necessary to understand the disk chemistry around massive stars. These observations will help us to reveal the massive star formation processes.

3.4. The Possibility of a Binary System

As shown in panel (a) of Figure 1, the two peaks with the separation of ~0.″1 are detected in the 1.38 mm continuum emission. Panel (a) of Figure 9 shows the *P–V* diagram of the H30α emission along a direction connecting the two continuum peaks (PA = −31°). It clearly shows that the H30α emission associated with the southeast peak is blueshifted by ~10 km s^{-1} from the northwest peak.

Moscadelli et al. (2021) interpreted this velocity gradient as the ionized disk rotation around a massive protostar. Assuming an edge-on orientation, they derived the dynamical mass of ~17 $M_\odot$, which should be the minimum mass considering the possible inclination. Consistent with this dynamical mass evaluation, Cesaroni et al. (2019) suggested an O9.5 star based on the derived Lyman continuum rate of 5.3×10^{47} s^{-1}. We also constructed the spectral energy distribution (SED) toward this source to retrieve the stellar mass and other physical properties, using infrared data from Spitzer, Wide-field Infrared Survey Explorer (WISE), and Herschel (Table 4 in Appendix C) and fitting the SED with the Zhang & Tan (2018) model (see Appendix C for the details). The best models of the SED fitting suggested the stellar masses of 16–24 $M_\odot$ with the bolometric luminosities of a few times 10^5 $L_\odot$ (see Figure 13 and Table 5 in Appendix C), which is also consistent with the dynamical mass estimation with the Keplerian disk by Moscadelli et al. (2021). The agreement of the independent analyses supports the presence of a ~20 $M_\odot$ star with the ionized-gas disk in the center of the G24 HC H II region.

However, this ionized disk scenario does not explain the presence of the two continuum peaks well. An alternative interpretation would be that the kinematic structure of H30α consists of two ionized disks associated with two massive

Table 4
Background-subtracted Flux Densities Derived at Each Wavelength for the SED Plot

Wavelength (μm)	Flux Density (Jy)
Spitzer	
3.6	0.02 (0.13)
4.5	0.20 (0.33)
8.0	0.58 (4.13)
24.0	6.81 (12.00)
WISE	
3.4	0.01 (0.08)
4.6	0.27 (0.43)
11.5	0.49 (5.31)
22.0	6.92 (30.06)
Herschel	
70.0	1352.47 (1539.58)
160.0	2046.43 (2487.86)
500.0	43.32 (86.73)

Note. The values in parenthesis are fluxes without the continuum subtraction. The photometric aperture radius was fixed at 16″, which was based on the 70 μm Herschel image.

Table 5
Parameters of the Five Best-fitted Models

χ^2	M_c ($M_\odot$)	Σ_{cl} (g cm^{-2})	R_c (pc)	m_* ($M_\odot$)	θ_{view} (°)	A_V (mag)	M_{env} ($M_\odot$)	$\theta_{w,esc}$ (°)	$\dot{M}_{disk}$ ($M_\odot$ yr^{-1})	$L_{bol,iso}$ ($L_\odot$)	L_{bol} ($L_\odot$)
1.11	480	3.160	0.09	24	13	361.92	440.54	12	2.0×10^{-3}	1.1×10^6	2.9×10^5
1.38	400	3.160	0.08	24	13	350.15	361.65	13	1.9×10^{-3}	1.3×10^6	3.0×10^5
1.93	320	3.160	0.07	24	13	325.19	276.82	15	1.8×10^{-3}	1.8×10^6	3.1×10^5
2.37	400	3.160	0.08	16	62	0.00	368.90	10	1.5×10^{-3}	8.8×10^4	1.0×10^5
2.72	480	1.000	0.16	24	22	217.99	433.43	15	8.2×10^{-4}	1.9×10^5	2.1×10^5

young stars orbiting around each other, i.e., a binary system. In fact, instead of one single velocity gradient across ∼0.″1, the *P*–*V* diagram appears to be more consistent with two separate components with the velocity offset (i.e., the orbital motion), each of which has its own velocity gradient (i.e., the rotation of each disk). It is worth briefly discussing the possibility of the binary system in G24, considering its asymmetric structures and the high binary rate of massive stars.

We can derive the total mass of the binary system assuming that the protostars locate at the continuum peaks and their velocity offset is due to the orbital motion. The peak separation is 0.″08 or $\Delta S \simeq 540$ au, which is a project separation. We estimate their velocity offset as $\Delta V \simeq 8.4\,\mathrm{km\,s^{-1}}$ from the H30α spectra at the peak locations (panel (b) of Figure 9). Considering a circular Kepler orbit, we derive the total dynamical mass as $M_{tot} = \Delta V^2 \Delta S/G \simeq 43\,M_\odot$, where G is the gravitational constant. This formula is different from that in the disk scenario by a factor of 8, i.e., $M_c = \Delta V^2 \Delta S/(8G)$ (where M_c is the stellar mass at the disk center; see Section 4.1 of Moscadelli et al. 2021), because ΔS represents the separation of the two sources while it is the diameter of the ionized disk in the disk scenario. Since free–free and H30α emissions trace the surrounding ionized gas rather than the protostar itself, the actual positions of the protostars might be slightly off the continuum emission peaks. Considering such ΔS uncertainty of ∼100 au (or 0.″015) and the ΔV fitting error of $0.36\,\mathrm{km\,s^{-1}}$, we estimate that the mass range of $M_{tot} \simeq 34$–$51\,M_\odot$ is consistent with the binary scenario. We note that the circular orbit perpendicular to the plane of sky are assumed here, and thus we consider those as the minimum masses.

The total values of the Lyman continuum rate and the infrared luminosity can also provide constraints on the stellar masses of the binary. Moscadelli et al. (2018) and Cesaroni et al. (2019) estimated a total Lyman continuum rate of $(5.3$–$7.2) \times 10^{47}\,\mathrm{s^{-1}}$ by fitting the radio to millimeter SED. As the two peaks have similar brightness in the continuum and H30α total emissions, the two massive stars in the binary should have similar masses, and therefore similar Lyman continuum rate of $\sim 3 \times 10^{47}\,\mathrm{s^{-1}}$. Such a Lyman continuum rate corresponds to a zero-age main-sequence (ZAMS) mass of $18\,M_\odot$, making a total mass of $36\,M_\odot$ for the binary, which is close to the minimum dynamical mass estimated above. If the binary stars have not reached the ZAMS phase, their masses can be higher because their Lyman continuum rate would be lower than those in the ZAMS phase at the same masses (e.g., Tanaka et al. 2016). As discussed in Appendix C, we conducted the infrared SED fitting. The mass estimation from this fitting is not applicable for the binary system because it assumed a single-star system. However, the obtained total bolometric luminosity of a few $\times 10^5\,L_\odot$ is reasonable even for the multiple-source system (Table 5). Considering the protostellar evolution, the luminosity of a massive protostar with ∼15–20 $M_\odot$ would be as bright as $10^5\,L_\odot$ (e.g., Zhang & Tan 2018), which is again consistent with the estimation of the dynamical mass.

The systemic velocity of G24 measured from the outer molecular emissions is $\sim 112\,\mathrm{km\,s^{-1}}$. If we assume that the line-of-sight velocity of the mass center of the binary is $112\,\mathrm{km\,s^{-1}}$, the mass ratio between the primary and secondary would be about 2:1 from the central velocity of each continuum peak. Considering the dynamical mass of $>37\ M_\odot$, we evaluate $\gtrsim 24\ M_\odot$ for A1-SE and $\gtrsim 12\ M_\odot$ for A1-NW. However, such analysis is susceptible to the determination of the line center velocities of H30α, which have FWHMs of 30–35 $\mathrm{km\,s^{-1}}$, as well as the binary system velocity. Therefore, it is still difficult to accurately determine the masses of the individual stars via dynamics.

We note that the binary scenario does not necessarily contradict the other features of G24. In the case of the binary star scenario, the rotating structure traced by CH_3CN and HC_3N is a circumbinary disk surrounding the two massive stars. The *P*–*V* diagrams of the molecular lines are roughly consistent with the Keplerian rotation with ∼20 $M_\odot$, but the disk is assumed to be perpendicular to the sky in these diagrams (Figure 3; Figure 4 of Moscadelli et al. 2021). Hence, the value of $20\,M_\odot$ is the minimum enclosed mass, and the total dynamical mass of $>37\ M_\odot$ from the H30α emission is acceptable. The presence of a single jet perpendicular to the molecular disk reported by Moscadelli et al. (2018, 2021) does not exclude the binary scenario. For example, in the forming massive binary system IRAS 16547–4247, one of the binary stars launches a single jet nearly perpendicular to the circumbinary disk, while the other star shows no jet feature, despite both protostars show almost the same levels of continuum and line emissions (Tanaka et al. 2020). If this is also happening in G24, one star may be supplied with more material from the circumstellar disk. Such an asymmetric infalling structure at <1000 au could cause the asymmetric UV field suggested in the larger scale.

Similar to the binary scenario for G24, Zhang et al. (2019b) reported a forming massive binary IRAS 07299–1651 with each member traced by hydrogen recombination lines showing velocity offset caused by orbital motion. In IRAS 07299–1651, the line emissions from the two stars are well separated that allows analyzing the circumstellar disk rotation of the primary star. However, in G24, the H30α emissions from the continuum peaks have already spread out and merged together, making it difficult to analyze the detailed kinematic structures of the ionized gas, i.e., the circumstellar disks and their circumbinary disk. We speculate that G24 is more massive than IRAS 07299–1651, and thus the ionized gas is more extended.

Therefore, although we suggest the possibility of the binary system in G24, we cannot confirm such a scenario with the current data set. Future higher-angular-resolution observations may help to confirm this point.

4. Conclusions

We have analyzed the ALMA archival data in Band 6 toward the G24 HC H II region. The vibrationally excited lines of HC_3N ($v_7 = 2$, $J = 24 - 23$) have been detected around the G24 HC H II region. The main results and conclusions of this paper are as follows.

1. We have compared the moment 0 map and the P–V diagram of the HC_3N ($v_7 = 2$, $J = 24 - 23$, $l = 2e$) line and the CH_3CN ($v_8 = 1$, $J_{K,l} = 12_{6,1} - 11_{6,1}$) line. Features in the spatial distributions and the P–V diagram of HC_3N are similar to those of CH_3CN. Thus, the HC_3N emission is tracing the molecular disk around the G24 HC H II region previously identified by the CH_3CN lines. These results indicate that the HC_3N emission can be used as a disk tracer for massive protostars even at the evolutionary stage of the HC H II region.
2. We have derived the column density ratios of $^{13}CH_3CN/HC^{13}CCN$ at the two representative regions, the central and molecular regions, which are determined based on the continuum map and the HC_3N moment 0 map, respectively. The ratios are derived to be 3.47 ± 0.46 and $3.10^{+3.68}_{-1.62}$ at the central and molecular regions, respectively. We have also derived the integrated-intensity ratios between the CH_3CN ($v_8 = 1$, $J_{K,l} = 12_{6,1} - 11_{6,1}$) and HC_3N ($v_7 = 2$, $J = 24 - 23$, $l = 2e$) lines and between the $^{13}CH_3CN$ ($J_K = 13_3 - 12_3$) and $HC^{13}CCN$ ($J = 26 - 25$) lines. All of the CH_3CN/HC_3N ratios derived based on integrated intensity and column density show the higher values at the central region than those at the molecular region. These results suggest that HC_3N is more efficiently destroyed in the region irradiated by the strong UV radiation.
3. We have compared the $^{13}CH_3CN/HC^{13}CCN$ abundance ratios around G24 to the CH_3CN/HC_3N abundance ratios in the disks around Herbig Ae and T Tauri stars. The abundance ratios around G24 are higher than those in the other disks by more than 1 order of magnitude. The difference between the G24 HC H II region and the other disks is caused by (1) efficient thermal desorption of CH_3CN in hot and dense region around the G24 HC H II region, and (2) rapid destruction of HC_3N in the region irradiated by the strong UV radiation around the G24 HC H II region.
4. Based on the two peaks of the free–free emission and their H30α kinematics in the central ionized region, we briefly discussed the possibility that it is composed of a binary system. We evaluated the total dynamical mass is $\gtrsim 37\ M_\odot$, which is consistent with the total bolometric luminosity and the Lyman continuum. However, we cannot confirm the binary scenario with the current data set. This is because the H30α emissions extended from the two continuum peaks merge in the position–velocity space, which makes the detailed dynamical analysis challenging.

We have shown that HC_3N can be used as a disk tracer even for massive protostars. The nitrile species, CH_3CN and HC_3N, are mainly formed by different formation processes (dust-surface reactions versus gas-phase reactions), and thus, the CH_3CN/HC_3N abundance ratio will be able to become a useful tracer for physical structures of disks around massive protostars. We need to increase source samples of massive stars as well as lower-mass stars, in order to understand the nitrile chemistry and the connection between physics and chemistry in disk structures.

This paper makes use of the following ALMA data: ADS/JAO.ALMA#2018.1.00745.S. ALMA is a partnership of ESO (representing its member states), NSF (USA), and NINS (Japan), together with NRC (Canada), MOST, and ASIAA (Taiwan), and KASI (Republic of Korea), in cooperation with the Republic of Chile. The Joint ALMA Observatory is operated by ESO, AUI/NRAO, and NAOJ. The National Radio Astronomy Observatory is a facility of the National Science Foundation operated under cooperative agreement by Associated Universities, Inc. Data analysis was in part carried out on the Multiwavelength Data Analysis System operated by the Astronomy Data Center (ADC), National Astronomical Observatory of Japan. We thank the anonymous referee whose valuable comments helped improve the paper.

K.T. appreciates the support by JSPS KAKENHI grant No. JP20K14523. K.T. thanks Dr. Yusuke Miyamoto (East Asian ALMA Regional Center/National Astronomical Observatory of Japan) for his kind support for our data reduction at the ADC. K.E.I.T. acknowledges the support by JSPS KAKENHI grant Nos. JP19K14760, JP19H05080, JP21H00058, and JP21H01145. R.F. acknowledges funding from the European Union's Horizon 2020 research and innovation program under the Marie Sklodowska-Curie grant agreement No. 101032092. J.C.T. acknowledges support from ERC project MSTAR and VR grant 2017-04522. S.T. is supported by JSPS KAKENHI grant Nos. JP21H00048 and JP21H04495. L.M. acknowledges the financial support of DAE and DST-SERB research grants (SRG/2021/002116 and MTR/2021/000864) of the Government of India.

Facility: Atacama Large Millimeter/submillimeter Array (ALMA).

Software: Common Astronomy Software Applications package (CASA; McMullin et al. 2007), Astropy (Astropy Collaboration et al. 2013, 2018); this research made use of Photutils, version 1.0.0, an Astropy package for detection and photometry of astronomical sources (Bradley et al. 2020).

Appendix A
Moment 0 Maps of the ^{13}C Isotopologues

Figure 10 shows moment 0 maps of $HC^{13}CCN$ and $^{13}CH_3CN$ toward the G24 HC H II region. We only show three lines of $^{13}CH_3CN$ ($J_K = 13_K - 12_K$, $K = 2$, 3, 6), because these lines are not contaminated by other lines.

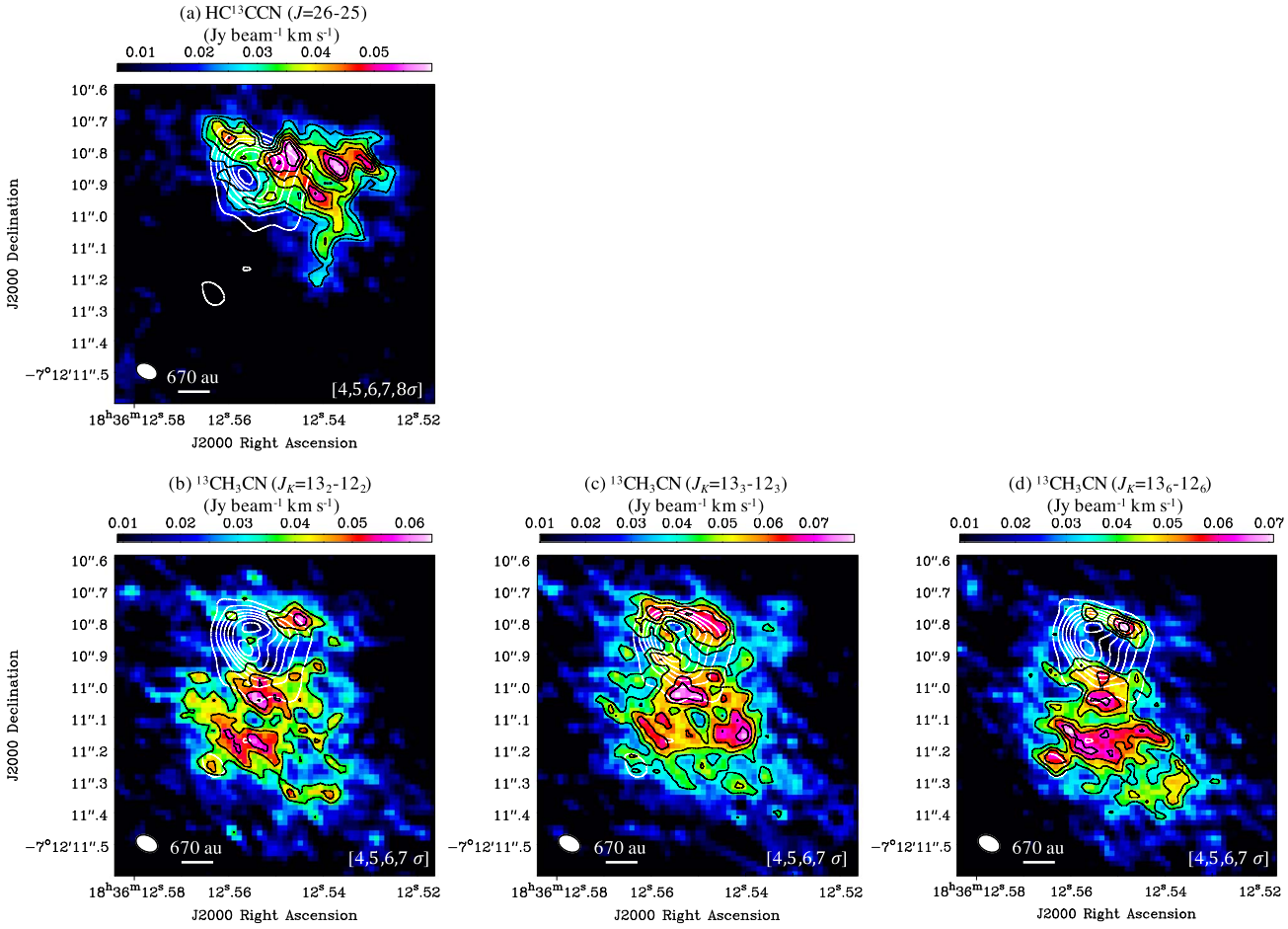

Figure 10. Moment 0 images of (a) $HC^{13}CCN$ ($J = 26 - 25$), (b) $^{13}CH_3CN$ ($J_K = 13_2 - 12_2$), (c) $^{13}CH_3CN$ ($J_K = 13_3 - 12_3$), and (d) $^{13}CH_3CN$ ($J_K = 13_6 - 12_6$), respectively. The rms noise levels are 7 mJy beam^{-1} km s^{-1} for panel (a), 9 mJy beam^{-1} km s^{-1} for panels (b) and (d), and 10 mJy beam^{-1} km s^{-1} for panel (c), respectively. The black contour levels are indicated in each panel. The white contours indicate the continuum image from 20σ to 80σ, in steps of 10σ. The filled white ellipses indicate angular resolution of $0\farcs068 \times 0\farcs048$ for panel (a), and $0\farcs074 \times 0\farcs051$ for the other panels, respectively. The linear scale is given for $0\farcs1$ corresponding to 670 au.

Appendix B
Channel Maps of the Vibrationally Excited Lines

Figures 11 and 12 show channel maps of the vibrationally excited lines of HC_3N ($v_7 = 2$, $J = 24 - 23$, $l = 2e$) and CH_3CN ($v_8 = 1$, $J_{K,l} = 12_{6,1} - 11_{6,1}$), respectively.

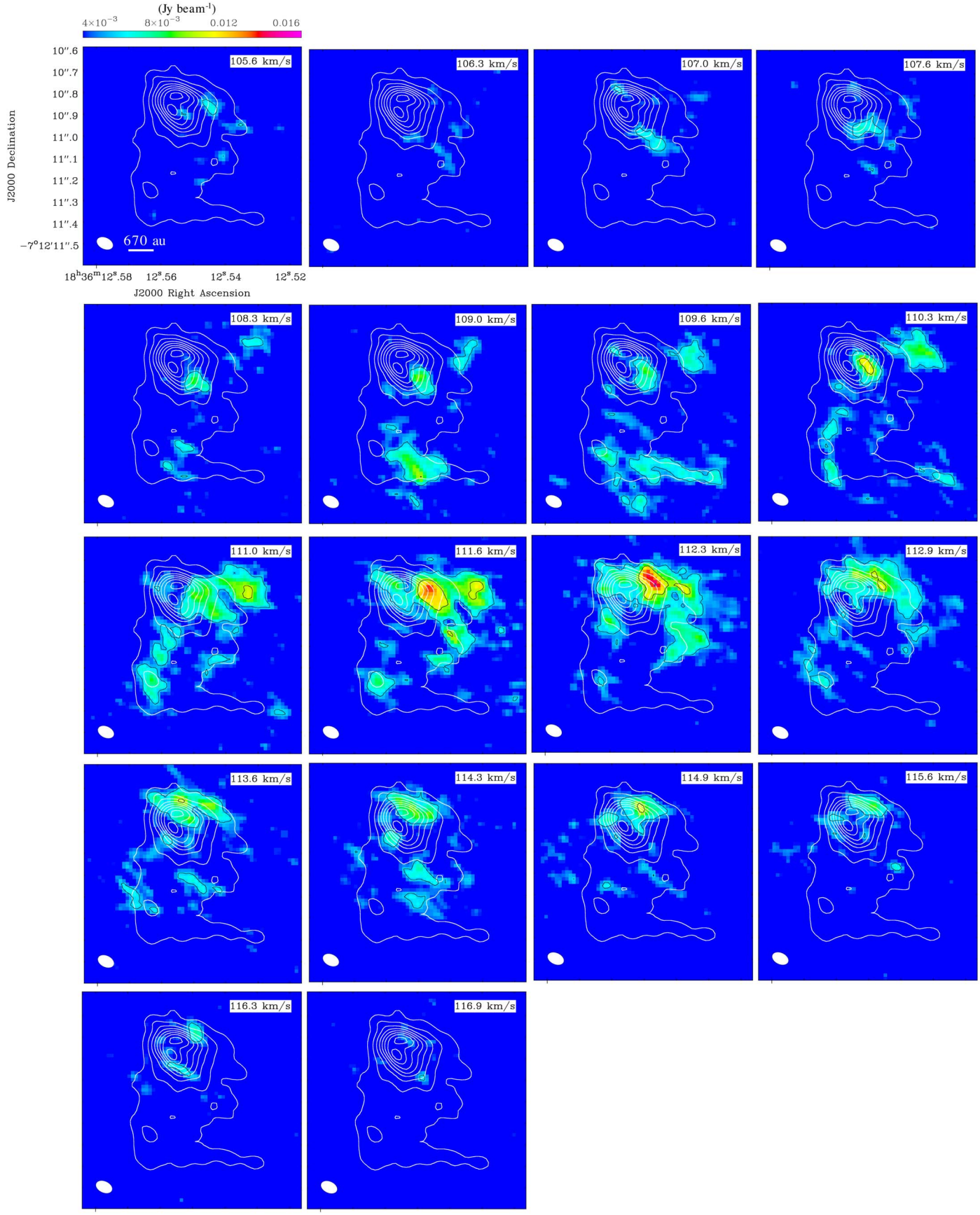

Figure 11. Channel maps of the HC_3N ($v_7 = 2$, $J = 24 - 23$, $l = 2e$) line ranging from 105.6 to 116.9 km s^{-1}. The black contours indicate the signal levels from 5σ in steps of 5σ. The noise level is 1.1 mJy beam^{-1}. The white contours indicate the continuum image from 10σ to 80σ, in steps of 10σ. The filled white ellipses indicate angular resolution of $0\farcs079 \times 0\farcs053$. The linear scale is given for $0\farcs1$ corresponding to 670 au.

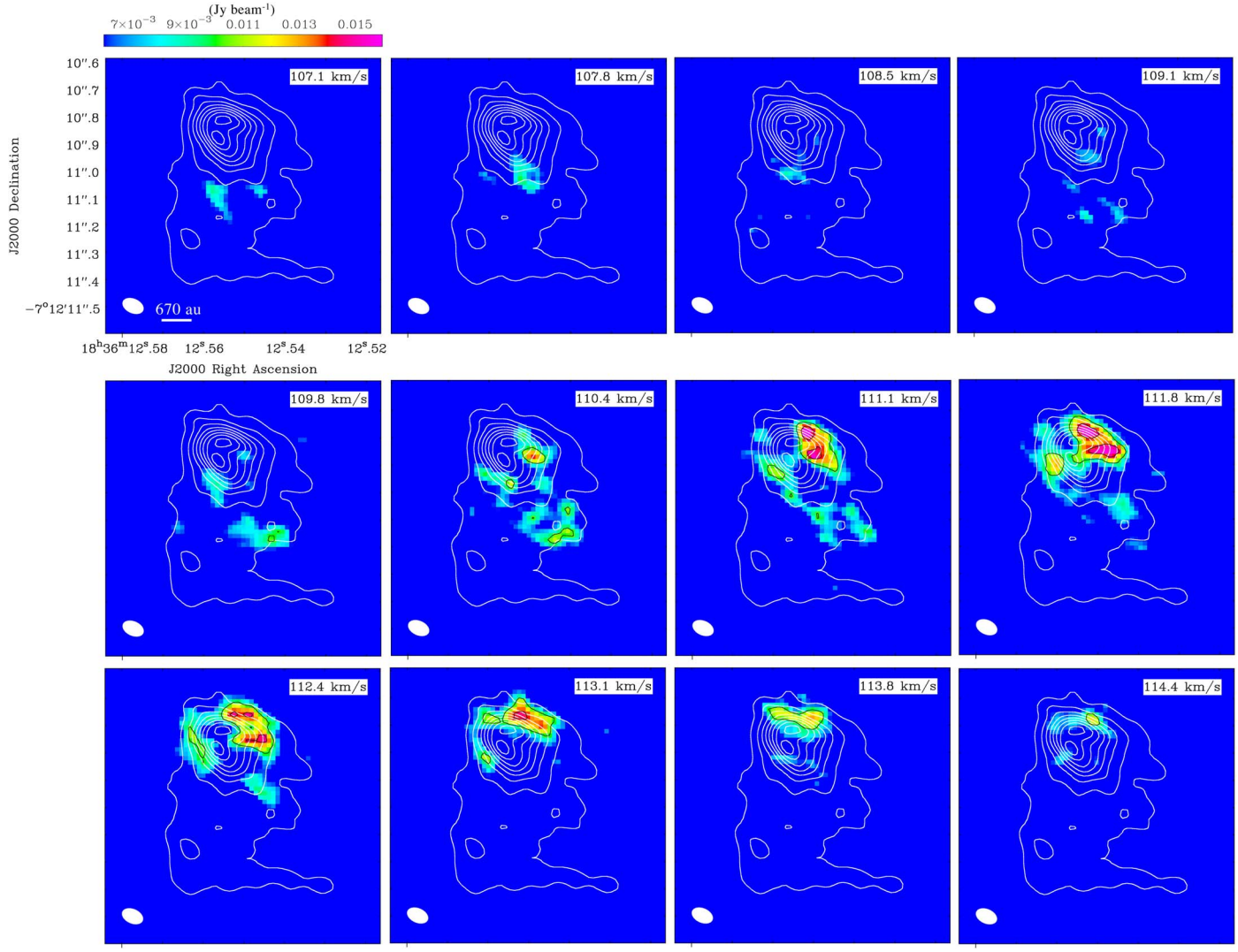

Figure 12. Channel maps of the CH_3CN ($v_8 = 1$, $J_{K,l} = 12_{6,1} - 11_{6,1}$) line ranging from 107.1 to 115.1 km s^{-1}. The black contours indicate the signal levels from 5σ in steps of 2σ. The noise level is 2.0 mJy beam^{-1}. The white contours indicate the continuum image from 10σ to 80σ, in steps of 10σ. The filled white ellipses indicate angular resolution of $0\farcs082 \times 0\farcs053$. The linear scale is given for $0\farcs1$ corresponding to 670 au.

Appendix C
SED Fitting Toward the G24 HC H II Region

In order to retrieve physical information from the HC H II region, we constructed the SED and subsequently fitted the Zhang & Tan (2018) model grid. We first measured the flux density in Spitzer, WISE, and Herschel data (Table 4). To do this, we performed circular aperture photometry fixing the aperture radius to $16''$ to all wavelengths, following the fiducial method in De Buizer et al. (2017) and Liu et al. (2019, 2020). The aperture size was chosen to enclose most of the flux in the 70 μm Herschel image and variations of 30% in the aperture radius to larger size did not affect significantly the final flux obtained. The standard method in performing circular aperture photometry also subtracts the background emission that is evaluated in an annulus from one to two aperture radii. The background-subtracted flux densities are reported in the second column of Table 4 and are the ones used in the SED fitting (we also report in the same column the flux densities without background subtraction in parenthesis). Once the fluxes were measured, we fitted to the SED model grid that provides estimates of key protostellar properties. We used the Zhang & Tan (2018) model grid and developed an improved version written in python called *sedcreator*[16] based on the original code written in IDL.[17] The details of this package will be publicly available in a forthcoming paper (R. Fedriani et al. 2022, in preparation). The Zhang & Tan (2018) model grid is based on the assumption that massive stars are formed from massive prestellar cores supported by internal pressure. The model grid self-consistently includes the evolutionary sequences of protostar, disk, envelope, and outflow cavity. The constrained free parameters of the model grid are: initial core mass (M_c), environmental clump mass surface density(Σ_{cl}), current protostellar mass (m_*), viewing angle with respect to the outflow axis (θ_{view}), and amount of foreground extinction (A_V).

By minimizing the χ^2 function defined in Equation (4) of Zhang & Tan (2018) for each physical model, we find that the best five models are consistent with a M_c ranging from 320 to 480 $M_\odot$, a Σ_{cl} with 1.0–3.16 g cm^{-2}, and most importantly a current protostellar mass of $16 - 24$ $M_\odot$ (Table 5). The intrinsic

[16] .https://github.com/fedriani/sedcreator or https://pypi.org/project/sedcreator/.
[17] https://zenodo.org/record/1134877#.YRJl4ZMza84

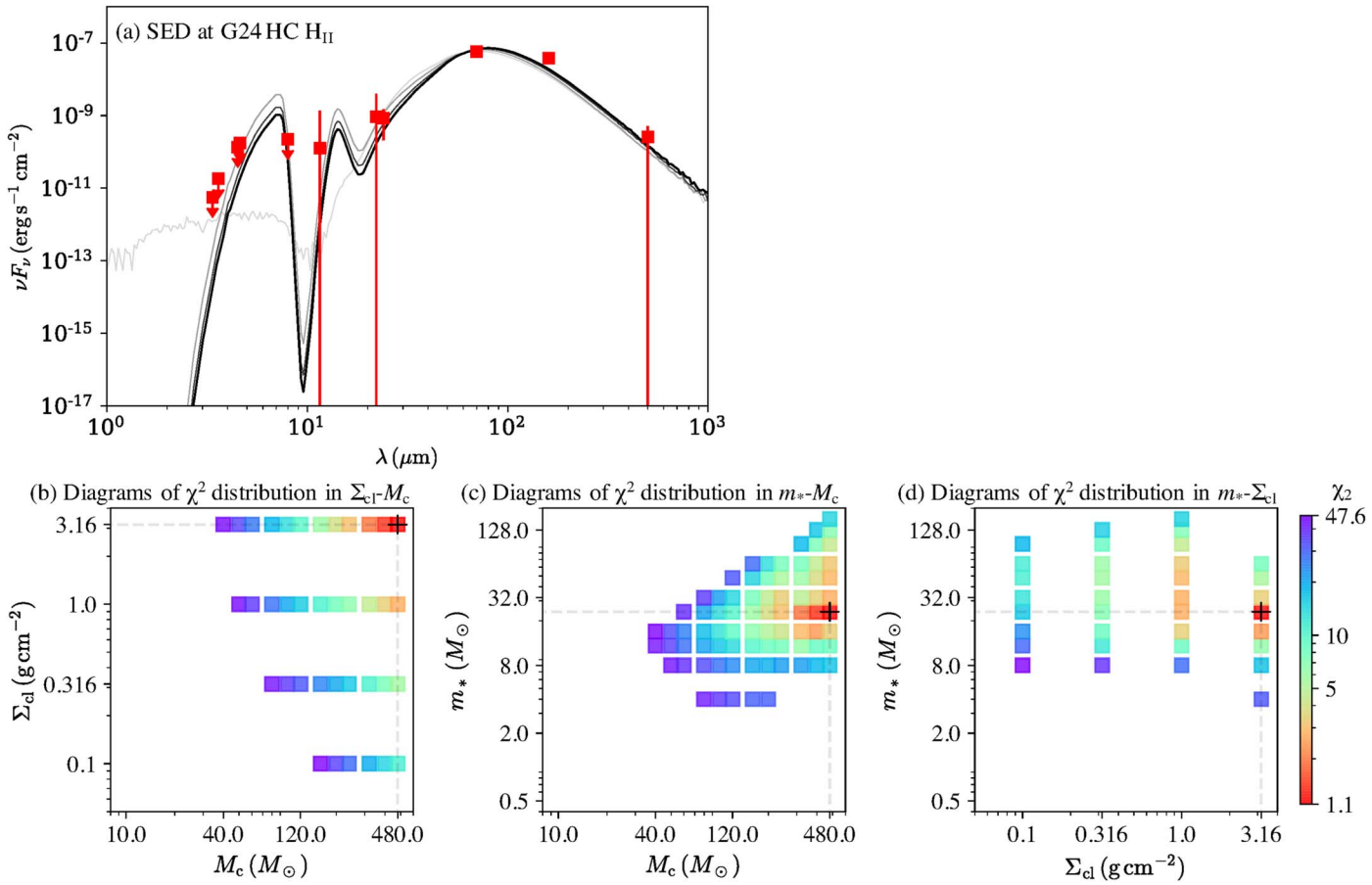

Figure 13. (a) SEDs of the five best models with the observations represented as red squares. The best-fit model is shown with a solid black line and the next four best models are shown with solid gray lines. (b)–(d) Diagrams of χ^2 distribution in Σ_{cl}–M_c space, m_*–M_c space, and m_*–Σ_{cl} space, respectively. The black crosses indicate the locations of the best model.

bolometric luminosity is also a few $\times 10^5$ $L_\odot$, i.e., which is the level associated with such massive protostars. This further supports the findings from the P–V analysis from the molecular emission. Panel (a) of Figure 13 shows the best five models, with the best model represented with thick black line, and the observations as red squares. The error bars are set to be the larger of either 10% of the clump background-subtracted flux density to account for calibration error, or the value of the estimated clump background flux density. Note that all data points below $\lambda < 8$ μm are treated as upper limits (see, e.g., De Buizer et al. 2017). Panels (b)–(d) of Figure 13 show the 2D distribution of the three main physical parameters, i.e., M_c, Σ_{cl}, and m_*.

ORCID iDs

Kotomi Taniguchi https://orcid.org/0000-0003-4402-6475
Kei E. I. Tanaka https://orcid.org/0000-0002-6907-0926
Yichen Zhang https://orcid.org/0000-0001-7511-0034
Rubén Fedriani https://orcid.org/0000-0003-4040-4934
Jonathan C. Tan https://orcid.org/0000-0002-3389-9142
Shigehisa Takakuwa https://orcid.org/0000-0003-0845-128X
Fumitaka Nakamura https://orcid.org/0000-0001-5431-2294
Masao Saito https://orcid.org/0000-0003-0769-8627
Liton Majumdar https://orcid.org/0000-0001-7031-8039
Eric Herbst https://orcid.org/0000-0002-4649-2536

References

Astropy Collaboration, Price-Whelan, A. M., Sipőcz, B. M., et al. 2018, AJ, 156, 123
Astropy Collaboration, Robitaille, T. P., Tollerud, E. J., et al. 2013, A&A, 558, A33
Bally, J., Ginsburg, A., Forbrich, J., et al. 2020, ApJ, 889, 178
Bergner, J. B., Guzmán, V. G., Öberg, K. I., et al. 2018, ApJ, 857, 69
Bonnell, I. A., Bate, M. R., Clarke, C. J., et al. 2001, MNRAS, 323, 785
Bradley, L., Sipőcz, B., Robitaille, T., et al. 2020, astropy/photutils: v1.0.1 Zenodo, doi:10.5281/zenodo.4049061
Caselli, P., & Ceccarelli, C. 2012, A&ARv, 20, 56
Cesaroni, R., Beltrán, M. T., Moscadelli, L., et al. 2019, A&A, 624, A100
Cesaroni, R., Sánchez-Monge, Á., Beltrán, M. T., et al. 2017, A&A, 602, A59
Cleeves, L. I., Bergin, E. A., Öberg, K. I., et al. 2017, ApJL, 843, L3
Crockett, N. R., Bergin, E. A., Neill, J. L., et al. 2014, ApJ, 787, 112
Csengeri, T., Bontemps, S., Wyrowski, F., et al. 2018, A&A, 617, A89
De Buizer, J. M., Liu, M., Tan, J. C., et al. 2017, ApJ, 843, 33
Gadhi, J., Lahrouni, A., Legrand, J., et al. 1995, JCP, 92, 1984
Goldsmith, P. F., & Langer, W. D. 1999, ApJ, 517, 209
Ilee, J. D., Cyganowski, C. J., Nazari, P., et al. 2016, MNRAS, 462, 4386
Ilee, J. D., Walsh, C., Booth, A. S., et al. 2021, ApJS, 257, 9
Johnston, K. G., Robitaille, T. P., Beuther, H., et al. 2015, ApJL, 813, L19
Jørgensen, J. K., Belloche, A., & Garrod, R. T. 2020, ARA&A, 58, 727
Le Gal, R., Brady, M. T., Öberg, K. I., et al. 2019, ApJ, 886, 86
Liu, M., Tan, J. C., De Buizer, J. M., et al. 2019, ApJ, 874, 16
Liu, M., Tan, J. C., De Buizer, J. M., et al. 2020, ApJ, 904, 75
Loomis, R. A., Cleeves, L. I., Öberg, K. I., et al. 2018, ApJ, 859, 131
Maud, L. T., Cesaroni, R., Kumar, M. S. N., et al. 2018, A&A, 620, A31
McKee, C. F., & Tan, J. C. 2002, Natur, 416, 59
McKee, C. F., & Tan, J. C. 2003, ApJ, 585, 850

McMullin, J. P., Waters, B., Schiebel, D., et al. 2007, Astronomical Data Analysis Software and Systems XVI, ASP Conf. Ser. 376, (Tuscon, AZ: Univ. Arizona Press), 127
Moscadelli, L., Cesaroni, R., Beltrán, M. T., et al. 2021, A&A, 650, A142
Moscadelli, L., Rivilla, V. M., Cesaroni, R., et al. 2018, A&A, 616, A66
Müller, H. S. P., Schlöder, F., Stutzki, J., et al. 2005, JMoSt, 742, 215
Öberg, K. I., Guzmán, V. V., Walsh, C., et al. 2021, ApJS, 257, 1
Pickett, H. M., Poynter, R. L., Cohen, E. A., et al. 1998, JQSRT, 60, 883
Sakai, N., Sakai, T., Hirota, T., et al. 2014, Natur, 507, 78
Sánchez-Monge, Á., Cesaroni, R., Beltrán, M. T., et al. 2013, A&A, 552, L10
Sanna, A., Giannetti, A., Bonfand, M., et al. 2021, A&A, 655, A72
Tan, J. C., Beltrán, M. T., Caselli, P., et al. 2014, Protostars and Planets VI (Tuscon, AZ: Univ. Arizona Press), 149
Tanaka, K. E. I., Tan, J. C., & Zhang, Y. 2016, ApJ, 818, 52
Tanaka, K. E. I., Tan, J. C., & Zhang, Y. 2017, ApJ, 835, 32
Tanaka, K. E. I., Zhang, Y., Hirota, T., et al. 2020, ApJL, 900, L2
Taniguchi, K., Guzmán, A. E., Majumdar, L., et al. 2020, ApJ, 898, 54
Taniguchi, K., Herbst, E., Caselli, P., et al. 2019a, ApJ, 881, 57
Taniguchi, K., Herbst, E., Majumdar, L., et al. 2021a, ApJ, 908, 100
Taniguchi, K., Majumdar, L., Takakuwa, S., et al. 2021b, ApJ, 910, 141
Taniguchi, K., Ozeki, H., & Saito, M. 2017, ApJ, 846, 46
Taniguchi, K., Saito, M., & Ozeki, H. 2016, ApJ, 830, 106
Taniguchi, K., Saito, M., Sridharan, T. K., et al. 2019b, ApJ, 872, 154
Wang, P., Li, Z.-Y., Abel, T., et al. 2010, ApJ, 709, 27
Wright, M., Plambeck, R., Hirota, T., et al. 2020, ApJ, 889, 155
Wyrowski, F., Schilke, P., & Walmsley, C. M. 1999, A&A, 341, 882
Zhang, Y., & Tan, J. C. 2018, ApJ, 853, 18
Zhang, Y., Tan, J. C., Sakai, N., et al. 2019a, ApJ, 873, 73
Zhang, Y., Tan, J. C., Tanaka, K. E. I., et al. 2019b, NatAs, 3, 517
Zhang, Y., Tanaka, K. E. I., Rosero, V., et al. 2019c, ApJL, 886, L4